

Task-Specific Knowledge Distillation from the Vision Foundation Model for Enhanced Medical Image Segmentation

Pengchen Liang^{†1,2}, Haishan Huang^{†3}, Bin Pu^{†4}, Jianguo Chen^{3*}, Xiang Hua³,
Jing Zhang⁵, Weibo Ma⁶, Zhuangzhuang Chen⁴, Yiwei Li^{7*}, Qing Chang^{1*}

¹Department Shanghai Key Laboratory of Gastric Neoplasms, Department of Surgery, Shanghai Institute of Digestive Surgery, Ruijin Hospital, Shanghai Jiao Tong University School of Medicine, Shanghai, 200025, China.

²School of Microelectronics, Shanghai University, Shanghai, 201800, China.

³School of Software Engineering, Sun Yat-sen University, Zhuhai, 519000, China.

⁴Department of Electronic and Computer Engineering, The Hong Kong University of Science and Technology, Hong Kong, SAR, China.

⁵Department of Radiology, Ruijin Hospital, Shanghai Jiaotong University School of Medicine, Shanghai, 200025, China.

⁶School of Public Administration, East China Normal University, Shanghai, 200062, China.

⁷Department of Nuclear Medicine, Shanghai Children’s Hospital, School of Medicine, Shanghai Jiao Tong University, Shanghai, 200062, China.

*Corresponding author(s). E-mail(s): chenjg33@mail.sysu.edu.cn;
liyawei@shchildren.com.cn; robie0510@hotmail.com;

Abstract

Large-scale pre-trained models, such as Vision Foundation Models (VFMs), have demonstrated impressive performance across various downstream tasks by transferring generalized knowledge, especially when target data is limited. However, their high computational cost and the domain gap between natural and medical images limit their practical application in medical segmentation tasks. Motivated by this, we pose the following important question: "How can we effectively utilize the knowledge of large pre-trained VFMs to train a small, task-specific model for medical image segmentation when training data is limited?" To address this problem, we propose a novel and generalizable task-specific knowledge distillation framework. Our method fine-tunes the VFM on the target segmentation task to capture task-specific features before distilling the knowledge to smaller models, leveraging Low-Rank Adaptation (LoRA) to reduce the computational cost of fine-tuning. Additionally, we incorporate synthetic data generated by diffusion models to augment the transfer set, enhancing model performance in data-limited scenarios. Experimental results across five medical image datasets demonstrate that our method consistently outperforms task-agnostic knowledge distillation and self-supervised pre-training approaches like MoCo v3 and Masked Autoencoders (MAE). For example, on the KidneyUS dataset, our method achieved a 28% higher Dice score than task-agnostic KD using 80 labeled samples for fine-tuning. On the CHAOS dataset, it achieved an 11% improvement over MAE with 100 labeled samples. These results underscore the potential of task-specific knowledge distillation to train accurate, efficient models for medical image segmentation in data-constrained settings.

Keywords: Medical image segmentation, Knowledge distillation, Vision Foundation Model (VFM), Self-supervised learning

1 Introduction

Medical image segmentation is essential for clinical diagnosis, treatment planning, and surgical guidance, as it enables precise delineation of anatomical structures and pathological regions [1–5]. Despite advances in deep learning, developing high-performance segmentation models remains challenging due to the scarcity of annotated medical data. Annotating medical images is costly and time-intensive, requiring specialized expertise to label complex structures [6] meticulously. This scarcity hampers the training of effective models, which typically require large amounts of labeled data to generalize well.

Vision Foundation Models (VFMs), pre-trained on extensive and diverse datasets, have emerged as promising tools by capturing generalized features transferable to various downstream tasks [7, 8]. These models have shown potential in medical image segmentation through transfer learning [9–12]. However, directly applying VFMs to medical imaging faces two significant challenges. *(1) The domain gap between natural images, on which VFMs are typically trained, and medical images limit their effectiveness due to differences in features and structures [13–15]. (2) VFMs are often large and computationally intensive, making them impractical for deployment in resource-constrained clinical environments.*

An effective solution is to transfer the knowledge of VFMs to smaller, task-specific models that are efficient and tailored for medical image segmentation. Knowledge distillation (KD) provides a framework for this transfer, where a large "teacher" model imparts its knowledge to a smaller "student" model [16–20]. Previous typical task-agnostic KD methods (Figure 1(Middle)) often focus on transferring generic feature representations without tailoring to the specific needs

of the target task [21]. These approaches may inadequately capture crucial features necessary for accurate segmentation, such as fine anatomical boundaries and subtle pathological variations, reducing the effectiveness of the smaller model.

To address these challenges, we propose a novel task-specific knowledge distillation framework (Figure 1(Bottom)) that effectively transfers knowledge from large pre-trained VFMs to smaller, efficient models tailored for medical image segmentation. Our framework first fine-tunes the VFM on the target segmentation task using the limited available labeled medical data. This fine-tuning enables the VFM to learn task-relevant features specific to medical images. We then distill this task-specific knowledge to a smaller model by aligning both the intermediate representations and the final segmentation outputs between the fine-tuned VFM and the small model. This process ensures that the small model inherits the critical features necessary for high-accuracy segmentation, overcoming the limitations of traditional KD approaches.

To reduce the computational cost associated with fine-tuning large VFMs, we employ Low-Rank Adaptation (LoRA) [22–25], which allows efficient adaptation of large models with minimal additional parameters. Furthermore, recognizing the scarcity of medical data, we leverage diffusion models [26–28] to generate synthetic medical images. These synthetic images augment the unlabeled transfer set (Figure 1(Top)) used during the knowledge distillation process, enhancing the diversity of training samples and enabling the small model to learn more effectively from the fine-tuned VFM in data-limited scenarios.

In our experiments, we also compare the effectiveness of our task-specific KD framework with self-supervised learning (SSL) approaches, which have emerged as an alternative to mitigate the need for large amounts of labeled data. SSL-based methods, such as Momentum Contrast (MoCo v3)[29] and Masked Autoencoders (MAE)[30], allow models to learn from unlabeled data by solving pretext tasks to learn useful representations. While these methods have demonstrated

[†]Pengchen Liang, Haishan Huang, and Bin Pu contributed equally to this work.

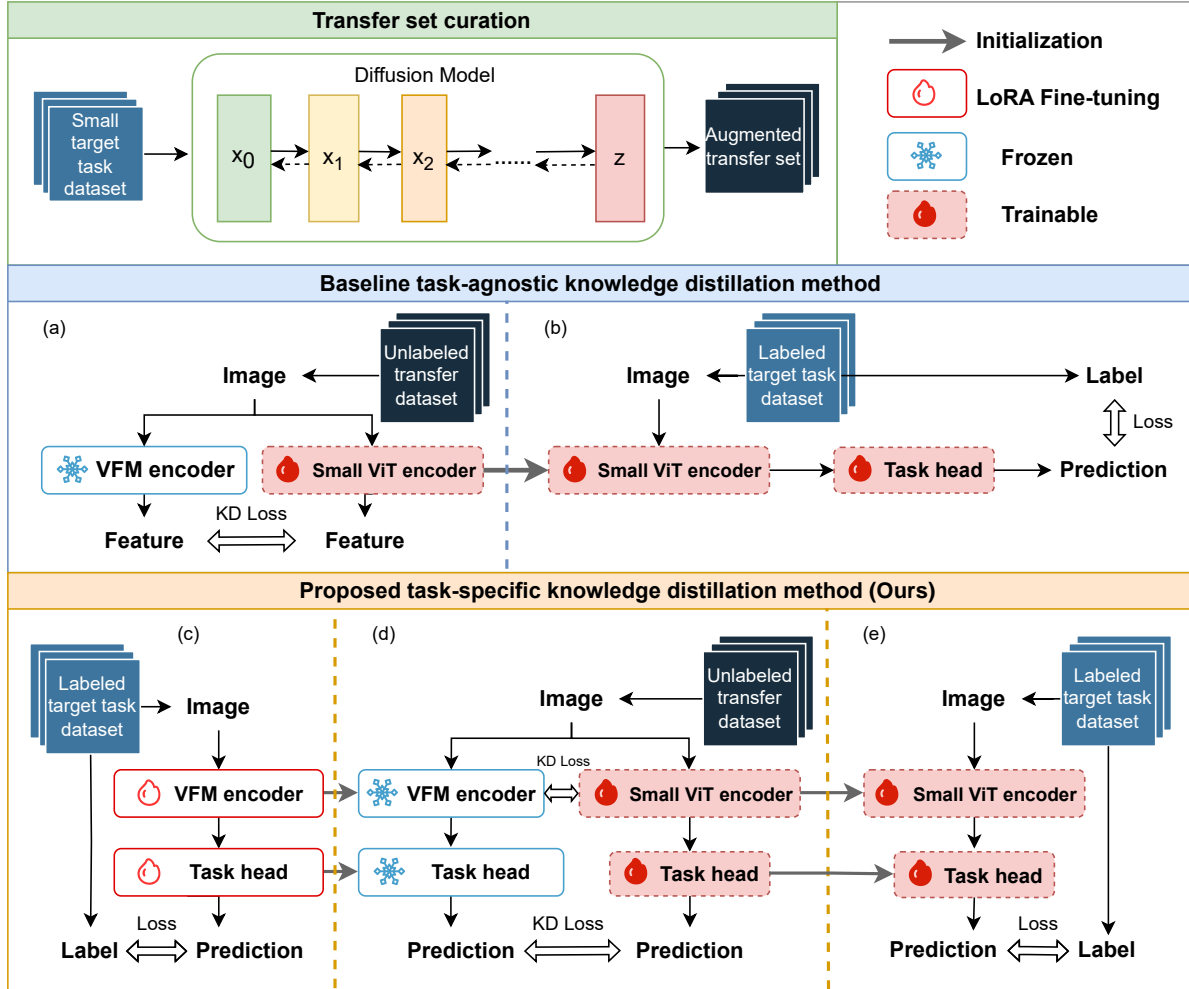


Fig. 1: Overview of the proposed task-specific knowledge distillation framework compared with the task-agnostic method. **Top:** Transfer set curation using a diffusion model to generate synthetic data from a small labeled dataset, expanding the training set. **Middle:** *Task-agnostic knowledge distillation method:* (a) The small Vision Transformer (ViT) model is pre-trained by matching its features to those extracted by the VFM on the unlabeled transfer set, focusing on general feature alignment. (b) The small ViT is fine-tuned using the labeled target task data. **Bottom:** *Proposed task-specific knowledge distillation method:* (c) The VFM is first fine-tuned on the target task using LoRA adaptation. (d) The small ViT model is pre-trained by aligning hidden layer representations and segmentation-specific predictions between the VFM and the small ViT on the unlabeled transfer set. (e) The small ViT model is fine-tuned using the labeled target task data to optimize segmentation performance.

success in medical image segmentation [31–34], we show that our task-specific KD framework consistently outperforms SSL methods in data-limited scenarios.

Our key contributions are as follows:

- We propose a task-specific KD framework that leverages fine-tuned VFM to transfer domain-specific knowledge to smaller Vision Transformer (ViT) models. By aligning hidden layer representations and segmentation outputs, our

method achieves more comprehensive and accurate knowledge transfer for medical image segmentation, overcoming the limitations of traditional KD approaches.

- To reduce the computational cost of fine-tuning large VFMs, we adopt LoRA, allowing for efficient adaptation of the VFM while preserving its large-scale pre-training benefits.
- We enhance the KD process by generating an augmented transfer set with diffusion models, increasing the diversity and size of the training data. Our analysis of different transfer set sizes (1,000; 2,000; and 3,000 synthetic images) shows that task-specific KD scales effectively with larger transfer sets, leading to significant performance improvements in data-limited segmentation tasks.
- We conduct a thorough evaluation of task-specific KD against state-of-the-art techniques, including task-agnostic KD and self-supervised pretraining methods such as MoCo v3 and MAE. Our experiments span various data-constrained settings, providing new insights into the relative performance of each approach across different medical segmentation tasks.
- Through extensive experiments on five diverse medical imaging datasets, we demonstrate that task-specific KD consistently outperforms competing methods, particularly in data-limited conditions. Notably, our approach achieves a 74.82% Dice score improvement in retinal vessel segmentation on the DRIVE dataset and a 13.59% improvement in kidney segmentation on the KidneyUS dataset, highlighting its robustness in complex segmentation tasks.

2 Related Work

2.1 Knowledge Distillation (KD)

Knowledge distillation (KD) has emerged as an effective approach for transferring knowledge from a large teacher model to a smaller student model, thereby reducing computational requirements while retaining performance. Various KD strategies have been explored over the years, including transferring logits from teacher to student [16], matching intermediate feature representations [35, 36], and utilizing attention maps [37, 38]. In the medical imaging domain, these methods have shown promise for enhancing performance,

especially when dealing with complex tasks such as segmentation. However, the use of task-specific KD for transferring detailed anatomical information remains under-explored, particularly in scenarios involving scarce labeled data. Recent research has also explored distillation in multi-modal settings such as image-language models [39, 40], but fewer works focus on the unique challenges presented by medical image segmentation. Our work investigates task-specific KD approaches, extending these traditional KD strategies by leveraging VFM, which is fine-tuned with task-relevant data for improved medical image segmentation.

2.2 Self-Supervised Learning and Transfer Learning

Self-supervised learning (SSL) has gained significant attention in medical image analysis, particularly due to the scarcity of labeled data. SSL methods, such as contrastive learning (e.g., MoCo v3 [29]) and reconstruction-based approaches like Masked Autoencoders (MAE) [30], have enabled models to learn useful representations from abundant unlabeled medical imaging data. SSL helps capture the underlying structures present in medical images, which is crucial for downstream tasks like segmentation. Transfer learning has also been extensively used in medical imaging, typically involving pretraining models on large-scale natural image datasets such as ImageNet [41]. Nevertheless, the domain gap between natural images and medical images can limit the generalization capabilities of these models [42]. By combining SSL with KD, our work leverages both representation learning from unlabeled datasets and task-specific knowledge transfer to achieve robust performance in medical image segmentation.

2.3 Task-Specific Knowledge Transfer in Vision Foundation Model

Vision Foundation Model (VFM), trained on diverse large-scale datasets, represents a significant advancement in image understanding across various domains, including medical imaging. Recent efforts, such as DINOv2 [7], have explored transferring knowledge from VFM in a task-agnostic manner, often using methods designed

for transformer architectures. Task-specific knowledge transfer, however, has received less attention in medical segmentation tasks, where domain-specific knowledge is vital for model accuracy. In our study, we focus on transferring knowledge from VFM that has been fine-tuned on specific segmentation tasks using methods like LoRA [22, 43]. We present a task-specific KD approach where the VFM is first fine-tuned on medical data, and the distilled knowledge is then transferred to a smaller Vision Transformer (ViT). Unlike traditional KD which often focuses on feature extraction, our approach aligns both feature representations and target predictions, ensuring a more comprehensive knowledge transfer. By constructing and evaluating transfer sets of different sizes, we demonstrate the benefits of this approach for efficient training in medical image segmentation, especially in data-scarce settings.

3 Methodology

3.1 Overview

In this work, we propose a generalizable task-specific knowledge distillation (TS-KD) framework for medical image segmentation, addressing data scarcity, efficient model adaptation, and comprehensive knowledge transfer. (1) A Swin-transformer-based diffusion model generates synthetic datasets to augment limited medical imaging data. (2) we fine-tune the Segment Anything Model (SAM) using Low-Rank Adaptation (LoRA), which efficiently adapts SAM’s parameters for task-specific segmentation needs. (3) Our dual-level distillation process aligns feature representations and segmentation outputs between SAM and a ViT-Tiny model, ensuring the effective transfer of both general and task-specific knowledge for improved segmentation performance in compact models.

3.2 Transfer Dataset Generation

To address the challenge of data scarcity in medical imaging, we used a Swin-transformer-based diffusion model to generate synthetic transfer datasets (Figure 1(TOP)). Each of the five primary datasets was augmented using data augmentation techniques (rotation, scaling, and affine transformations) to create a dataset of 1,000

images per task. These augmented datasets were then used to train the diffusion model for generating additional synthetic images.

The diffusion model is based on the research [44], utilizing a Swin-transformer-based network that employs a forward Gaussian noise process and a reverse denoising process. The forward process gradually adds noise to the input images over multiple time steps:

$$q(x_t|x_{t-1}) = \mathcal{N}(x_t; \sqrt{\alpha_t}x_{t-1}, (1 - \alpha_t)I), \quad (1)$$

where x_t represents the noisy image at time step t , and α_t is the noise scaling factor. The reverse process attempts to predict and denoise the noisy images to generate realistic synthetic images:

$$p_\theta(x_{t-1}|x_t) = \mathcal{N}(x_{t-1}; \mu_\theta(x_t, t), \sigma_t^2 I), \quad (2)$$

where $\mu_\theta(x_t, t)$ is the predicted mean by the model with parameters θ , and σ_t^2 is the variance of the noise.

3.3 Task-Specific Knowledge Distillation (KD)

As shown in Figure 2, we proposed a Task-Specific Knowledge Distillation (KD) framework combined with LoRA Fine-Tuning to effectively transfer knowledge from a large SAM model to a smaller ViT-Tiny model for segmentation tasks. This approach aims to distill both general and task-specific knowledge, ensuring that the student model learns both the encoder’s feature extraction capabilities and the decoder’s task-specific outputs.

3.3.1 LoRA Fine-Tuning of the SAM Model

To adapt the large SAM model to the target segmentation task, we use LoRA (Low-Rank Adaptation) for fine-tuning both the SAM encoder and decoder (as illustrated in Figure 2b). LoRA enables efficient adaptation by injecting trainable low-rank matrices into the model’s attention layers, reducing the number of parameters that need to be updated while preserving most of the original model’s knowledge.

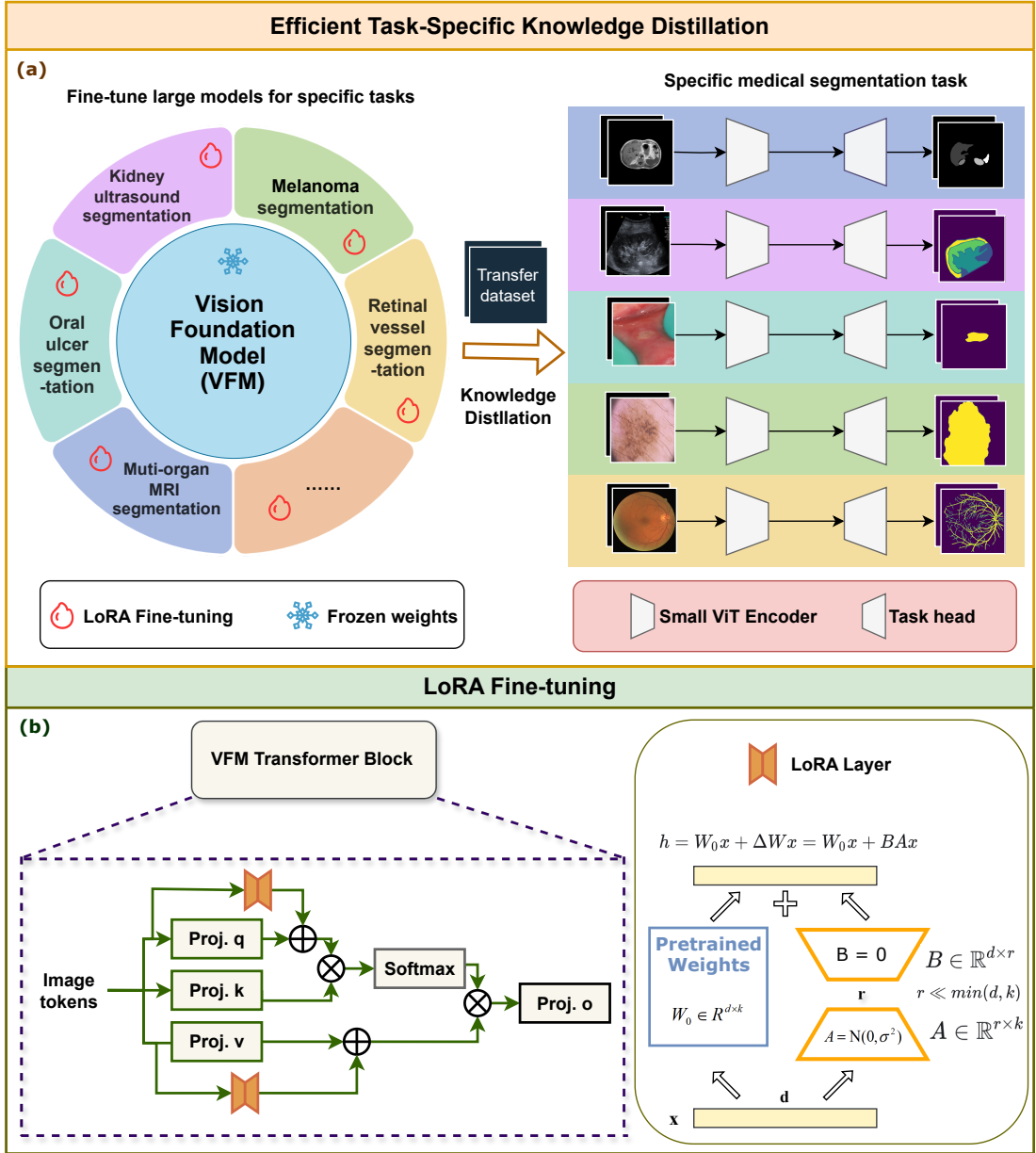


Fig. 2: Efficient Task-Specific Knowledge Distillation framework. (a) Fine-tuning large models for specific medical segmentation tasks, such as kidney ultrasound, melanoma, and retinal vessel segmentation, using the Vision Foundation Model (‘Segment Anything Model’). The framework utilizes LoRA fine-tuning to adapt VFM’s encoder and decoder for these specific tasks. Transfer datasets are used in combination with knowledge distillation to train smaller task-specific models for efficient deployment. (b) Detailed architecture of LoRA fine-tuning, showing the VFM transformer’s block with LoRA layers for efficient parameter updates, where pre-trained weights are kept frozen while low-rank matrices adjust the attention mechanism to fit the target task.

For each attention weight matrix $W_0 \in \mathbb{R}^{d \times d}$ in the SAM model, LoRA introduces two low-rank matrices $A \in \mathbb{R}^{d \times r}$ and $B \in \mathbb{R}^{r \times d}$, where $r \ll d$, and modifies the original weight matrix as follows:

$$W = W_0 + \Delta W, \quad \Delta W = A \cdot B, \quad (3)$$

where ΔW is the task-specific adaptation, and r is a hyperparameter controlling the adaptation’s rank. This technique allows us to fine-tune only the added low-rank matrices A and B , while keeping the original weights W_0 frozen, enabling efficient task-specific adaptation of the SAM model.

Detail technique of LoRA.

The LoRA fine-tuning was conducted on both the query and value projection layers of each transformer block within the SAM model’s encoder. Freezing the remaining parameters of the SAM model ensures minimal update overhead. Following settings in [43], the AdamW optimizer was used with an initial learning rate of 0.005, and the fine-tuning process utilized a warmup strategy to stabilize the early training stages. The warmup period was set to 250 iterations, with a maximum of 160 epochs for training. The cross-entropy loss and Dice loss were combined in a 0.2 : 0.8 ratio to supervise the fine-tuning process:

$$L = \lambda_1 \text{CE}(S, \hat{S}) + \lambda_2 \text{Dice}(S, \hat{S}), \quad (4)$$

where $\lambda_1 = 0.2$ and $\lambda_2 = 0.8$ control the balance between the two loss components.

3.3.2 Dual-Level Knowledge Distillation

To transfer knowledge from the fine-tuned SAM model to the ViT-Tiny model, we adopt a dual-level knowledge distillation strategy that aligns both the encoder’s hidden representations and the decoder’s output predictions.

Encoder in KD.

We match the hidden representations from the final layers of the encoders in the student and teacher models, allowing the student model (ViT-Tiny) to learn from the rich feature representations of the SAM model. The distillation loss is given by:

$$\mathcal{L}_{KD}^{encoder} = \frac{1}{N} \sum_{i=1}^N \|h_i^{(student)} - h_i^{(teacher)}\|^2, \quad (5)$$

where N is the number of feature map elements, and $h_i^{(student)}$ and $h_i^{(teacher)}$ are the hidden states from the student and teacher encoders, respectively.

Decoder in KD.

To transfer task-specific knowledge, we also align the outputs of the student and teacher decoders. Specifically, the output logits of the SAM decoder (producing low-resolution segmentation masks) are matched with the final output of the ViT-Tiny decoder. The distillation loss for this process is given by:

$$\mathcal{L}_{KD}^{decoder} = \frac{1}{M} \sum_{j=1}^M \|y_j^{(student)} - y_j^{(teacher)}\|^2, \quad (6)$$

where $y_j^{(student)}$ and $y_j^{(teacher)}$ represent the predicted segmentation logits, and M is the number of elements (pixels) in the segmentation mask.

3.4 Theoretical Derivations

In this section, we present a mathematical analysis to substantiate the theoretical advantages of Task-Specific Knowledge Distillation (TS-KD) over Task-Agnostic Knowledge Distillation (TA-KD). By employing principles from PAC learning theory and information theory, we demonstrate how TS-KD leads to reduced generalization error and greater sample efficiency, especially in data-scarce scenarios like medical image segmentation.

3.4.1 Generalization Error in Knowledge Distillation

Given a student model F_S trained via distillation from a teacher model F_T , the generalization error can be expressed as:

$$R(F_S) = \mathbb{E}_{(x,y) \sim \mathcal{D}}[\ell(F_S(x), y)], \quad (7)$$

where $\ell(\cdot, \cdot)$ is the task-specific loss function (e.g., cross-entropy or Dice loss). In knowledge distillation, the goal is to minimize the divergence

between the student and teacher outputs while also ensuring that the student model generalizes well to the underlying task. The total error can be decomposed as:

$$R(F_S) = \text{Bias}^2(F_S) + \text{Variance}(F_S). \quad (8)$$

3.4.2 Hypothesis Space and VC Dimension

In distillation, the complexity of the hypothesis space \mathcal{H} that the student model explores plays a crucial role in determining generalization performance. Let the VC dimension $\text{VCdim}(\mathcal{H})$ represent the complexity of the hypothesis space. For a given training set size m , PAC learning bounds the generalization error as:

$$R(F_S) \leq \hat{R}_m(F_S) + O\left(\sqrt{\frac{\text{VCdim}(\mathcal{H})}{m}}\right), \quad (9)$$

where $\hat{R}_m(F_S)$ is the empirical error on the training data. In TS-KD, since the teacher model F_T^{LoRA} has been fine-tuned for the specific task, the student model’s hypothesis space \mathcal{H}_{TS} is naturally more restricted, leading to a lower VC dimension compared to TA-KD:

$$\text{VCdim}(\mathcal{H}_{\text{TS}}) < \text{VCdim}(\mathcal{H}_{\text{TA}}). \quad (10)$$

This reduction in hypothesis space complexity directly implies better generalization for TS-KD, as the generalization bound becomes tighter with fewer training examples.

3.4.3 Sample Complexity

In PAC learning, the sample complexity required to achieve a generalization error of at most ϵ with high probability $1 - \delta$ is given by:

$$m \geq O\left(\frac{1}{\epsilon^2} \left(\text{VCdim}(\mathcal{H}) + \ln \frac{1}{\delta}\right)\right). \quad (11)$$

Since $\text{VCdim}(\mathcal{H}_{\text{TS}}) < \text{VCdim}(\mathcal{H}_{\text{TA}})$, TS-KD requires fewer training examples to reach the same level of generalization, making it particularly advantageous when dealing with limited labeled data, as is common in medical imaging tasks.

3.4.4 Information-Theoretic Analysis

From an information-theoretic perspective, the effectiveness of knowledge distillation can be evaluated through the lens of information gain. The mutual information between the teacher’s output and the true label y provides insight into how well the teacher’s predictions guide the student:

$$I(T; Y) = H(Y) - H(Y|T), \quad (12)$$

In TA-KD, the teacher F_T is not fine-tuned for the task, which increases the entropy $H(T)$ of its output. Consequently, the mutual information $I(T; Y)$ is lower compared to TS-KD, where the teacher model F_T^{LoRA} is task-specific:

$$I(T^{\text{LoRA}}; Y) > I(T; Y). \quad (13)$$

This implies that TS-KD provides greater information gain for the student model, leading to better task performance and lower generalization error.

Through PAC learning and information-theoretic analysis, we have demonstrated that TS-KD offers significant theoretical advantages over TA-KD. By reducing the hypothesis space complexity and increasing the mutual information between the teacher’s output and the true label, TS-KD ensures better generalization with fewer training examples, making it particularly suitable for data-limited domains such as medical imaging.

4 Experiment

4.1 Experimental Setup

To comprehensively evaluate the effectiveness of the proposed task-specific knowledge distillation (KD) strategy for medical image segmentation, we designed experiments involving six distinct model groups, assessing various pre-training and fine-tuning strategies for lightweight models. This section describes the experimental setup, including datasets, model configurations, procedures, and evaluation metrics.

4.1.1 Datasets

We utilized five primary datasets to address different segmentation challenges in medical imaging, covering diverse modalities such as ultrasound,

oral cavity, abdominal, dermoscopic, and retinal images. These datasets enable a robust evaluation of our method’s generalizability and effectiveness:

- **KidneyUS Dataset [45]:** This ultrasound dataset focuses on kidney segmentation, with pixel-wise annotations delineating kidney regions. The images, sized at 512×512 , present challenges due to ultrasound noise and anatomical variability, testing the robustness of segmentation models in a low-contrast setting.
- **Autooral Dataset [46]:** This dataset provides images of the oral cavity for ulcer segmentation, with masks marking ulcerated regions. With 256×256 resolution, it challenges models with varying lighting conditions and complex anatomical structures within the oral cavity.
- **CHAOS Dataset [47]:** A benchmark dataset for multi-organ segmentation in abdominal MRI, containing organs like the liver, kidneys, and spleen, at 256×256 resolution. It assesses models’ adaptability in segmenting organs with complex shapes and low-contrast boundaries.
- **PH2 Dataset [48]:** This dermoscopic dataset, with images at 512×512 , is designed for skin lesion segmentation, including melanomas. The dataset provides a high-resolution view, essential for capturing fine details in texture and asymmetry to distinguish pathological regions.
- **DRIVE Dataset [49]:** A retinal fundus image dataset used for vessel segmentation, providing 512×512 images with vascular structure labels. This dataset evaluates the model’s precision in segmenting intricate vascular patterns, critical for detecting eye conditions like diabetic retinopathy.

4.1.2 Model Architectures

The models used in our experiments were based on Vision Transformer (ViT) architectures:

- **Vision Foundation Model (VFM).** We adopted the ViT-B model from SAM as the teacher model for KD. This model is a vision foundation model pre-trained on diverse datasets to capture robust visual representations. For task-specific knowledge distillation, we fine-tuned the SAM model on the labeled portion of each target dataset using Low-Rank Adaptation (LoRA).

- **Small ViT Model.** The student model was based on a ViT-Tiny [50] architecture, which was designed to be resource-efficient for deployment. The segmentation head in this model was built using a Feature Pyramid Network (FPN). The FPN takes the output from the last layer of the ViT-Tiny encoder, performs multi-scale feature aggregation, and generates the segmentation output. This model served as the student in KD and underwent multiple training strategies, including training from scratch, self-supervised pre-training, and knowledge distillation.

4.1.3 Baseline Pre-Training Strategies

We conducted experiments across different training groups to evaluate various pre-training techniques:

1. **ImageNet Pre-trained Small ViT Model with MAE.** Instead of training the model from scratch, we used pre-trained weights from the work [51], where the ViT tiny model was pre-trained on the ImageNet dataset using Masked Autoencoders (MAE). These pre-trained weights were then fine-tuned on our labeled target dataset. Due to the difference in input image size, we did not load the first layer of tokens when initializing the ViT-Tiny model, as the number of tokens differed from those in the original pre-training.
2. **Self-Supervised Pre-training with MoCo v3.** We applied Momentum Contrast (MoCo v3) for self-supervised pre-training on an unlabeled transfer dataset of varying sizes (1,000, 2,000, and 3,000 images). The MoCo v3 objective involves maintaining consistency between a query and a momentum-averaged key encoder:

$$\mathcal{L}_{MoCo} = -\log \frac{\exp(q \cdot k_+ / \tau)}{\sum_{i=0}^K \exp(q \cdot k_i / \tau)}, \quad (14)$$

where q is the query, k_+ is the positive key, k_i are negative keys, and τ is the temperature parameter.

3. **Self-Supervised Pre-training with MAE.** In this group, we employed Masked Autoencoders for self-supervised pre-training, following the same transfer datasets as in the MoCo experiments. This allowed us to compare the

effectiveness of different self-supervised learning techniques. The MAE pre-training objective involves reconstructing the original image from a masked version:

$$\mathcal{L}_{MAE} = \frac{1}{N} \sum_{i=1}^N \|x_i - f_{\theta}(\tilde{x}_i)\|^2, \quad (15)$$

where x_i is the original image, \tilde{x}_i is the masked image, and f_{θ} is the MAE model.

4. **Task-Agnostic Knowledge Distillation (KD).** In this approach, we performed knowledge distillation from only the SAM encoder to the ViT-Tiny encoder. The distillation loss function minimizes the mean squared error (MSE) between the hidden representations from the last hidden layers of the SAM and ViT-Tiny encoders:

$$\mathcal{L}_{KD}^{encoder} = \frac{1}{N} \sum_{i=1}^N \|h_i^{(student)} - h_i^{(teacher)}\|^2, \quad (16)$$

where $h_i^{(student)}$ and $h_i^{(teacher)}$ represent the hidden representations from the student and teacher encoders, respectively.

4.2 Training Procedure

For all training strategies, we followed a consistent procedure to ensure comparability:

- **Pre-training.** Pre-training (either self-supervised or through knowledge distillation) was performed on the synthetic transfer dataset. We used the AdamW optimizer with a learning rate schedule that included linear warm-up followed by cosine decay. Pre-training was conducted for 1,600 epochs.
- **Fine-tuning.** After pre-training, ViT tiny models were fine-tuned on the labeled portion of the target dataset using three different data scales.

4.2.1 Pre-Training Details

Our pre-training setup follows the established practices for MAE and MoCo-v3, with certain adjustments tailored to the lightweight ViT-Tiny model. Key details regarding batch sizes and other parameters are described below.

For MAE pre-training, we used a batch size of 64. The training was conducted with the AdamW

optimizer, starting with a base learning rate of 1.5×10^{-4} and a weight decay of 0.05. The learning rate followed a cosine decay schedule, with the pre-training carried out for 1600 epochs. This configuration is based on the setup recommended [51].

For MoCo-v3 pre-training, we adopted a batch size of 32, again using the AdamW optimizer but with a slightly higher weight decay of 0.1. The base learning rate was set at 1.5×10^{-4} , with a momentum coefficient of 0.99 and a temperature parameter of 0.2. Similar to MAE, a cosine learning rate schedule was used, and the pre-training was run for 1600 epochs, following the protocol described [51].

In the Knowledge Distillation (KD) pre-training, we utilized a batch size of 48. The student model was trained using the Adam optimizer with a base learning rate of 1.5×10^{-4} and a weight decay of 0.05. The learning rate followed a cosine decay schedule, and training was conducted for 1600 epochs to ensure sufficient convergence. This setup allowed us to effectively distill the knowledge from the SAM model into the smaller ViT-Tiny model for medical segmentation tasks.

All pre-training procedures were run on two NVIDIA L40 (48G) GPUs, which provided ample memory and computational power to handle the large-scale data and long training epochs efficiently.

4.2.2 ViT-Tiny Fine-Tuning Details

The ViT-Tiny model was fine-tuned using 160 epochs, with a batch size of 6 per GPU, and training distributed across 2 GPUs. A base learning rate of 1×10^{-4} was applied and the AdamW optimizer was selected for fine-tuning. For reproducibility, deterministic training was enabled, and a random seed of 1234 was set. Additionally, the loss function was a combination of cross-entropy loss and Dice loss, with a weighting of 0.2 for cross-entropy and 0.8 for Dice.

4.2.3 Evaluation Metrics

We employed the following metrics to evaluate segmentation performance:

- **Dice Similarity Coefficient (DSC).** Measures the overlap between the predicted and

ground truth segmentation masks:

$$DSC = \frac{2|A \cap B|}{|A| + |B|}, \quad (17)$$

where A and B represent the predicted and ground truth segmentation regions, respectively.

- **Hausdorff Distance 95 (HD95)**. Measures the distance between the predicted and reference boundaries, providing insight into the model’s ability to delineate structures accurately:

$$HD_{95} = \max\{\sup_{a \in A} \min_{b \in B} d(a, b), \sup_{b \in B} \min_{a \in A} d(a, b)\}, \quad (18)$$

where $d(a, b)$ is the Euclidean distance between points a and b .

- **Mean Intersection over Union (mIoU)**. Quantifies the agreement between predicted and reference segmentation regions:

$$mIoU = \frac{1}{C} \sum_{c=1}^C \frac{|A_c \cap B_c|}{|A_c \cup B_c|}, \quad (19)$$

where C represents the number of classes, and A_c and B_c are the predicted and ground truth regions for class c .

4.3 Effectiveness of Task-specific Knowledge Distillation

4.3.1 Performance Improvement

The effectiveness of our proposed Task-Specific Knowledge Distillation (KD) approach is thoroughly evaluated through extensive experiments on multiple medical image segmentation datasets, demonstrating notable performance improvements across all evaluated metrics and dataset types. Our method consistently outperformed both self-supervised and task-agnostic strategies, particularly under limited labeled data conditions, which is a common challenge in medical imaging. The results, summarized in Figure 3, Figure 4, Figures 5 to 9, and Tables 1–5, demonstrate that transferring domain-specific knowledge from large pre-trained Vision Foundation Models (VFMs) significantly enhances segmentation quality, even when only a small number of labeled examples are available for fine-tuning.

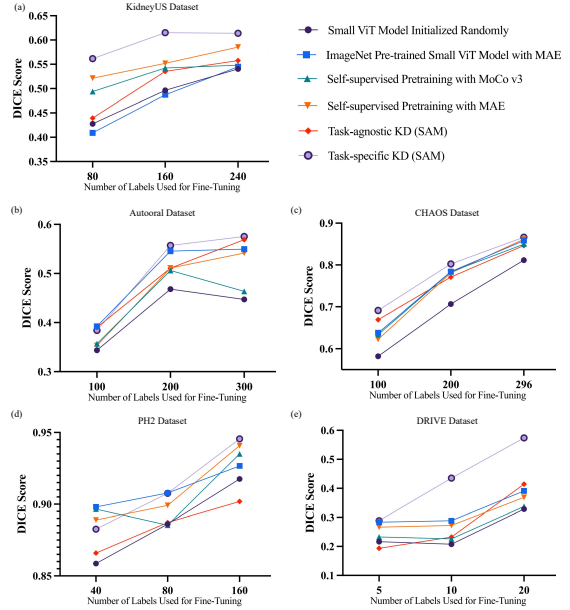


Fig. 3: Comparison of Dice scores across five medical imaging datasets (KidneyUS, Autooral, CHAOS, PH2, and DRIVE) using different pre-training and knowledge distillation methods. Each plot (a)-(e) represents a dataset, with results shown for models fine-tuned with varying numbers of labeled samples. Approaches include a Small ViT model trained from scratch, ImageNet pre-trained Small ViT model with MAE, self-supervised pretraining with MoCo v3 and MAE, task-agnostic knowledge distillation (KD), and task-specific KD (TS-KD). Task-specific KD consistently demonstrates the highest performance trends and superior Dice scores across all datasets, showcasing its effectiveness in leveraging task-relevant features for medical image segmentation.

As shown in Figure 3, the Dice scores for five datasets (KidneyUS, Autooral, CHAOS, PH2, and DRIVE) illustrate the consistent superiority of Task-Specific KD across different datasets and label counts. Each subplot in Figure 3 (a)-(e) visualizes segmentation performance trends, with Task-Specific KD consistently achieving the highest Dice scores compared to other methods, including task-agnostic KD and self-supervised approaches (MoCo v3, MAE). This advantage is particularly evident as the number of labeled samples increases, suggesting that Task-Specific KD effectively adapts the pre-trained model to

Table 1: Segmentation performance comparison for KidneyUS dataset across different methods, label counts, and transfer strategies

Method Description	Transfer Data Scale	Number of Labels	Capsule		Medulla		Central Echo Complex		Cortex		Mean	
			Dice	HD95 (mm)	Dice	HD95 (mm)	Dice	HD95 (mm)	Dice	HD95 (mm)	Dice	HD95 (mm)
Small ViT Model Initialized Randomly	-	80	0.3655	7.2093	0.5632	10.3342	0.4979	10.8743	0.2841	19.7758	0.4277	12.0484
Small ViT Model Initialized Randomly	-	160	0.4327	6.7461	0.6365	8.0982	0.5351	15.3710	0.3809	34.5692	0.4963	16.1961
Small ViT Model Initialized Randomly	-	240	0.4616	7.9583	0.7092	6.7958	0.5653	20.4725	0.4347	36.1479	0.5404	17.8436
ImageNet Pre-trained Small ViT Model with MAE	-	80	0.3665	6.2406	0.5104	11.7478	0.4597	14.6055	0.2999	25.2298	0.4091	14.4559
ImageNet Pre-trained Small ViT Model with MAE	-	160	0.4134	7.3575	0.6569	7.1722	0.5160	20.3646	0.3626	27.0141	0.4872	15.4771
ImageNet Pre-trained Small ViT Model with MAE	-	234	0.4765	7.4467	0.7134	5.7069	0.5917	19.0227	0.3980	25.4239	0.5449	14.4000
Self-supervised Pretraining with MoCo v3	1000	80	0.4124	6.8898	0.6368	7.0569	0.5233	10.2319	0.3885	25.3417	0.4902	12.3801
Self-supervised Pretraining with MoCo v3	1000	160	0.4427	8.0606	0.6839	6.5766	0.5349	15.9801	0.4279	33.7038	0.5223	16.0803
Self-supervised Pretraining with MoCo v3	1000	234	0.4649	7.7077	0.7033	8.0482	0.5731	17.9010	0.4491	34.0744	0.5476	16.9328
Self-supervised Pretraining with MoCo v3	2000	80	0.3725	8.4055	0.6144	10.7335	0.5155	11.6220	0.3952	21.9065	0.4744	13.1669
Self-supervised Pretraining with MoCo v3	2000	160	0.4515	10.3645	0.6812	7.9620	0.5428	20.7462	0.4303	31.1468	0.5264	17.5549
Self-supervised Pretraining with MoCo v3	2000	234	0.4834	6.6549	0.7108	5.5959	0.5645	25.7674	0.4582	41.8553	0.5542	19.9684
Self-supervised Pretraining with MoCo v3	3000	80	0.4293	6.2612	0.6466	6.6445	0.5095	11.9636	0.3901	25.4097	0.4939	12.5697
Self-supervised Pretraining with MoCo v3	3000	160	0.4656	7.1728	0.6937	6.9899	0.5578	15.2916	0.4521	26.6148	0.5423	14.0173
Self-supervised Pretraining with MoCo v3	3000	234	0.4783	6.7157	0.6989	6.7271	0.5604	15.8952	0.4547	35.5760	0.5481	16.2388
Self-supervised Pretraining with MAE	1000	80	0.3913	7.1131	0.6365	7.6220	0.5128	10.9918	0.3915	23.2192	0.4830	12.2590
Self-supervised Pretraining with MAE	1000	160	0.4897	7.1530	0.7162	5.1490	0.5678	13.1309	0.4465	29.6672	0.5550	13.7750
Self-supervised Pretraining with MAE	1000	234	0.5057	5.6074	0.7053	5.0298	0.5948	11.9608	0.4903	28.4184	0.5740	12.7616
Self-supervised Pretraining with MAE	2000	80	0.4560	5.6679	0.6820	5.2166	0.5435	11.7664	0.4185	24.1365	0.5250	11.6968
Self-supervised Pretraining with MAE	2000	160	0.5079	6.2690	0.7296	5.0700	0.5921	14.4391	0.5019	26.6200	0.5829	13.1010
Self-supervised Pretraining with MAE	2000	234	0.5121	5.3276	0.7276	6.2224	0.6075	18.6415	0.4800	36.9887	0.5818	16.7950
Self-supervised Pretraining with MAE	3000	80	0.4329	5.8616	0.6884	4.9088	0.5431	12.1240	0.4212	30.6463	0.5214	13.8522
Self-supervised Pretraining with MAE	3000	160	0.4730	7.3598	0.7152	5.6462	0.5674	14.1410	0.4516	26.5356	0.5518	13.4206
Self-supervised Pretraining with MAE	3000	234	0.5088	6.3253	0.7275	5.7195	0.6107	22.2091	0.4949	37.0393	0.5855	17.8233
Task-agnostic KD (SAM)	1000	80	0.3544	15.1931	0.5558	8.2828	0.4529	13.3010	0.2879	19.7221	0.4127	14.1247
Task-agnostic KD (SAM)	1000	160	0.4529	5.3973	0.6806	5.2860	0.5622	11.7397	0.4271	17.3085	0.5307	9.9329
Task-agnostic KD (SAM)	1000	234	0.4791	6.3924	0.7134	5.9355	0.6079	14.3139	0.4756	18.8792	0.5690	11.3802
Task-agnostic KD (SAM)	2000	80	0.3936	6.9990	0.5711	6.3886	0.4898	7.9029	0.3624	21.1759	0.4542	10.6166
Task-agnostic KD (SAM)	2000	160	0.4217	8.2424	0.6778	6.9117	0.5698	9.3997	0.4374	15.2620	0.5267	9.9539
Task-agnostic KD (SAM)	2000	234	0.4543	7.6766	0.7172	6.3631	0.6127	14.2856	0.4673	24.7729	0.5629	13.2745
Task-agnostic KD (SAM)	3000	80	0.3457	10.1499	0.5876	8.9912	0.4906	14.3876	0.3340	20.7546	0.4395	13.5708
Task-agnostic KD (SAM)	3000	160	0.4634	7.3193	0.6877	5.7065	0.5579	9.8316	0.4321	22.7944	0.5353	11.4130
Task-agnostic KD (SAM)	3000	234	0.4669	8.0206	0.7104	5.0995	0.5839	15.5131	0.4695	28.4162	0.5577	14.2624
Task-specific KD (SAM)	1000	80	0.4042	8.6556	0.6283	8.0949	0.5394	12.3679	0.4202	21.2673	0.4980	12.5964
Task-specific KD (SAM)	1000	160	0.4864	6.3202	0.7037	5.8052	0.5908	12.3019	0.4650	24.0490	0.5615	12.1193
Task-specific KD (SAM)	1000	234	0.5040	6.4866	0.7315	5.0885	0.6211	10.1459	0.4781	25.2262	0.5837	11.7368
Task-specific KD (SAM)	2000	80	0.4243	7.4113	0.6855	6.8013	0.5974	11.3959	0.4767	21.0418	0.5460	11.6626
Task-specific KD (SAM)	2000	160	0.4892	10.8606	0.7513	5.0694	0.6285	10.0007	0.5190	25.5534	0.5970	12.8710
Task-specific KD (SAM)	2000	234	0.5226	6.1660	0.7575	4.8903	0.6268	13.6789	0.5118	33.8565	0.6047	14.6479
Task-specific KD (SAM)	3000	80	0.4519	7.3774	0.7198	5.7491	0.6049	12.7213	0.4699	28.5719	0.5616	13.9049
Task-specific KD (SAM)	3000	160	0.5201	6.8427	0.7640	5.0911	0.6509	10.0121	0.5260	25.0108	0.6152	11.7392
Task-specific KD (SAM)	3000	234	0.5396	6.0549	0.7615	5.6710	0.6301	17.2060	0.5242	37.6263	0.6139	16.6395

Table 2: Segmentation performance comparison for Autooral dataset across different methods, label counts, and transfer strategies.

Method Description	Transfer Data Scale	Number of Labels	Dice	HD95 (mm)	mIoU
Small ViT Model Initialized Randomly	-	100	0.3437	31.7691	0.2099
Small ViT Model Initialized Randomly	-	200	0.4681	13.5781	0.3075
Small ViT Model Initialized Randomly	-	300	0.4470	18.4517	0.2906
ImageNet Pre-trained Small ViT Model with MAE	-	100	0.3924	19.1570	0.2471
ImageNet Pre-trained Small ViT Model with MAE	-	200	0.5457	10.0470	0.3775
ImageNet Pre-trained Small ViT Model with MAE	-	300	0.5495	12.7095	0.3860
Self-supervised Pretraining with MoCo v3	1000	100	0.3454	28.5079	0.2147
Self-supervised Pretraining with MoCo v3	1000	200	0.4784	12.1181	0.3183
Self-supervised Pretraining with MoCo v3	1000	300	0.4838	15.7585	0.3214
Self-supervised Pretraining with MoCo v3	2000	100	0.3548	26.4034	0.2223
Self-supervised Pretraining with MoCo v3	2000	200	0.4501	13.8809	0.2953
Self-supervised Pretraining with MoCo v3	2000	300	0.5244	12.6348	0.3575
Self-supervised Pretraining with MoCo v3	3000	100	0.3569	26.8678	0.2228
Self-supervised Pretraining with MoCo v3	3000	200	0.5061	11.1896	0.3418
Self-supervised Pretraining with MoCo v3	3000	300	0.4636	16.7257	0.3049
Self-supervised Pretraining with MAE	1000	100	0.3671	23.2796	0.2288
Self-supervised Pretraining with MAE	1000	200	0.5074	10.2626	0.3418
Self-supervised Pretraining with MAE	1000	300	0.4833	14.8763	0.3231
Self-supervised Pretraining with MAE	2000	100	0.3466	23.4145	0.2135
Self-supervised Pretraining with MAE	2000	200	0.5016	11.4486	0.3373
Self-supervised Pretraining with MAE	2000	300	0.5060	14.1237	0.3425
Self-supervised Pretraining with MAE	3000	100	0.3530	23.8724	0.2180
Self-supervised Pretraining with MAE	3000	200	0.5112	11.7949	0.3457
Self-supervised Pretraining with MAE	3000	300	0.5416	14.1652	0.3751
Task-agnostic KD (SAM)	1000	100	0.3112	39.6611	0.1874
Task-agnostic KD (SAM)	1000	200	0.5295	11.1319	0.3629
Task-agnostic KD (SAM)	1000	300	0.5116	11.8314	0.3462
Task-agnostic KD (SAM)	2000	100	0.2709	42.6107	0.1575
Task-agnostic KD (SAM)	2000	200	0.5447	9.8448	0.3752
Task-agnostic KD (SAM)	2000	300	0.5563	14.8505	0.3891
Task-agnostic KD (SAM)	3000	100	0.3902	22.1350	0.2445
Task-agnostic KD (SAM)	3000	200	0.5109	10.4191	0.3432
Task-agnostic KD (SAM)	3000	300	0.5688	13.2210	0.4011
Task-specific KD (SAM)	1000	100	0.2710	44.6681	0.1577
Task-specific KD (SAM)	1000	200	0.5176	10.0185	0.3513
Task-specific KD (SAM)	1000	300	0.5320	16.2647	0.3655
Task-specific KD (SAM)	2000	100	0.3997	27.8693	0.2554
Task-specific KD (SAM)	2000	200	0.5308	13.7065	0.3617
Task-specific KD (SAM)	2000	300	0.5739	9.0618	0.4054
Task-specific KD (SAM)	3000	100	0.3840	24.8617	0.2413
Task-specific KD (SAM)	3000	200	0.5570	12.3943	0.3873
Task-specific KD (SAM)	3000	300	0.5754	9.5722	0.4078

target-specific features, enabling robust performance gains even under limited supervision.

Figures 5 to 9 further illustrate the robustness and adaptability of Task-Specific KD in various experimental settings, including different scales of

transfer datasets and varying numbers of labeled samples for fine-tuning. Unlike other pre-training or KD methods, Task-Specific KD shows a stable improvement trend in segmentation performance as both the transfer dataset size and the number of

Table 3: Segmentation performance comparison for CHAOS dataset across different methods, label counts, and transfer strategies.

Method Description	Transfer Data Scale	Number of Labels	Liver		Right kidney		Left kidney		Spleen		Mean HD95 (mm)	
			Dice	HD95 (mm)	Dice	HD95 (mm)	Dice	HD95 (mm)	Dice	HD95 (mm)		
Small ViT Model Initialized Randomly	-	100	0.7693	5.5767	0.5608	13.8418	0.4947	17.1834	0.5030	9.1395	0.5820	11.4354
Small ViT Model Initialized Randomly	-	200	0.8368	3.1703	0.7225	8.8742	0.6693	12.1535	0.5972	9.1598	0.7065	8.3395
Small ViT Model Initialized Randomly	-	296	0.8605	2.7508	0.8111	12.2382	0.7960	8.3848	0.7779	3.3689	0.8114	5.6857
ImageNet Pre-trained Small ViT Model with MAE	-	100	0.7920	4.2662	0.5959	21.8129	0.5827	25.1126	0.5806	18.2058	0.8788	17.3494
ImageNet Pre-trained Small ViT Model with MAE	-	200	0.8697	2.5372	0.7952	5.3321	0.7785	8.3748	0.6931	9.1503	0.8414	6.3486
ImageNet Pre-trained Small ViT Model with MAE	-	296	0.9033	1.8482	0.8462	18.8943	0.8454	1.8960	0.8380	1.7443	0.8582	6.0957
Self-supervised Pretraining with MoCo v3	1000	100	0.7773	6.0554	0.6465	13.4479	0.6096	10.9569	0.6083	7.7831	0.6604	9.5608
Self-supervised Pretraining with MoCo v3	1000	200	0.8623	2.5078	0.7935	12.6678	0.7735	3.5502	0.6740	4.6776	0.7758	5.8508
Self-supervised Pretraining with MoCo v3	1000	296	0.8897	1.9529	0.8458	13.4999	0.8617	1.6344	0.8273	1.5475	0.8561	4.6587
Self-supervised Pretraining with MoCo v3	2000	100	0.7830	5.3652	0.6325	14.3418	0.5872	7.4772	0.5791	8.1382	0.6454	8.8906
Self-supervised Pretraining with MoCo v3	2000	200	0.8598	2.5396	0.8043	11.6902	0.7780	3.8273	0.7085	4.5071	0.7877	5.6410
Self-supervised Pretraining with MoCo v3	2000	296	0.8794	2.7385	0.8296	11.0511	0.8237	2.8962	0.8406	1.5954	0.8433	4.5703
Self-supervised Pretraining with MoCo v3	3000	100	0.7849	6.3558	0.5759	9.1804	0.5741	20.9508	0.6010	15.9590	0.6340	13.0205
Self-supervised Pretraining with MoCo v3	3000	200	0.8653	2.2300	0.8102	9.3535	0.7634	3.9993	0.6950	5.1697	0.7835	5.1881
Self-supervised Pretraining with MoCo v3	3000	296	0.8883	1.8826	0.8350	5.7061	0.8436	1.9512	0.8323	1.8316	0.8498	2.8428
Self-supervised Pretraining with MAE	1000	100	0.7525	5.7867	0.6120	19.0609	0.5724	8.4410	0.5503	8.3927	0.6218	10.4203
Self-supervised Pretraining with MAE	1000	200	0.8675	2.1202	0.8057	9.5423	0.7568	4.2687	0.6563	6.2919	0.7716	5.5558
Self-supervised Pretraining with MAE	1000	296	0.8968	1.5646	0.8513	12.5040	0.8684	1.5363	0.8218	1.5572	0.8596	4.2905
Self-supervised Pretraining with MAE	2000	100	0.7716	5.4694	0.6285	17.2058	0.5702	6.5626	0.5702	8.7602	0.6332	9.9658
Self-supervised Pretraining with MAE	2000	200	0.8662	2.4220	0.8151	5.8541	0.7619	3.6599	0.6504	6.0036	0.7734	4.4849
Self-supervised Pretraining with MAE	2000	296	0.8922	1.6961	0.8436	4.3005	0.8512	1.9431	0.8173	1.8150	0.8511	2.4387
Self-supervised Pretraining with MAE	3000	100	0.7737	5.1132	0.6072	13.8431	0.5873	12.8300	0.5217	8.8912	0.6225	10.1694
Self-supervised Pretraining with MAE	3000	200	0.8644	2.3210	0.8151	9.4634	0.7595	3.9868	0.6842	4.6321	0.7808	5.1008
Self-supervised Pretraining with MAE	3000	296	0.8949	1.6104	0.8599	5.9369	0.8596	1.7662	0.8320	2.2472	0.8616	2.8902
Task-agnostic KD (SAM)	1000	100	0.7707	5.8344	0.5570	17.5271	0.5381	15.0197	0.5140	8.5396	0.5949	11.7352
Task-agnostic KD (SAM)	1000	200	0.8541	2.9345	0.7877	6.9505	0.7126	4.8224	0.5636	6.7372	0.7295	5.6186
Task-agnostic KD (SAM)	1000	296	0.8660	2.9500	0.8222	11.8148	0.7760	6.4879	0.7723	3.2491	0.8091	6.1254
Task-agnostic KD (SAM)	2000	100	0.7816	5.6084	0.6520	8.0163	0.5776	6.5231	0.5987	10.1386	0.6525	7.5716
Task-agnostic KD (SAM)	2000	200	0.8549	2.5096	0.7849	4.6061	0.7363	4.6355	0.7097	4.9271	0.7714	4.1696
Task-agnostic KD (SAM)	2000	296	0.8901	1.7761	0.8289	9.6494	0.7873	6.0078	0.8043	3.0402	0.8276	5.1184
Task-agnostic KD (SAM)	3000	100	0.8148	3.5402	0.6083	6.9156	0.6451	6.9969	0.6091	8.5912	0.6693	6.5110
Task-agnostic KD (SAM)	3000	200	0.8614	2.3853	0.7854	4.3403	0.7169	10.8823	0.7202	4.0245	0.7710	5.4981
Task-agnostic KD (SAM)	3000	296	0.8951	1.9655	0.8707	6.2104	0.8226	2.4966	0.7862	2.8998	0.8465	4.3331
Task-specific KD (SAM)	1000	100	0.7143	8.9982	0.4552	24.1114	0.4710	11.7937	0.4797	13.2323	0.5301	14.5339
Task-specific KD (SAM)	1000	200	0.8527	2.8638	0.8018	17.0426	0.7492	4.2884	0.6416	6.6472	0.7613	7.7105
Task-specific KD (SAM)	1000	296	0.8756	2.2492	0.8370	17.1348	0.8347	1.8824	0.7520	4.3335	0.8248	6.4050
Task-specific KD (SAM)	2000	100	0.8062	7.9082	0.6675	23.7361	0.6689	8.3831	0.5511	8.9143	0.6734	12.2354
Task-specific KD (SAM)	2000	200	0.8647	2.3534	0.8128	8.8304	0.7948	3.4737	0.7126	4.7102	0.7962	4.8419
Task-specific KD (SAM)	2000	296	0.8993	1.8150	0.8543	14.4520	0.8567	1.6340	0.8300	1.6208	0.8601	4.8804
Task-specific KD (SAM)	3000	100	0.8541	7.6012	0.6588	22.6214	0.6417	15.7047	0.6305	8.4952	0.6912	11.1206
Task-specific KD (SAM)	3000	200	0.8757	2.0883	0.8258	9.7684	0.8016	3.6914	0.7068	4.7201	0.8025	5.0670
Task-specific KD (SAM)	3000	296	0.8955	2.0779	0.8553	11.8028	0.8680	1.3695	0.8463	1.4954	0.8663	4.1864

Table 4: Segmentation performance comparison for PH2 dataset across different methods, label counts, and transfer strategies.

Method Description	Transfer Data Scale	Number of Labels	Dice	HD95 (mm)	mIoU
Small ViT Model Initialized Randomly	-	40	0.8586	6.3603	0.7609
Small ViT Model Initialized Randomly	-	80	0.8862	3.0000	0.7970
Small ViT Model Initialized Randomly	-	160	0.9176	2.0000	0.8488
ImageNet Pre-trained Small ViT Model with MAE	-	40	0.8980	2.8680	0.8162
ImageNet Pre-trained Small ViT Model with MAE	-	80	0.9078	2.0000	0.8324
ImageNet Pre-trained Small ViT Model with MAE	-	160	0.9266	1.5590	0.8634
Self-supervised Pretraining with MoCo v3	1000	40	0.8851	2.7500	0.7960
Self-supervised Pretraining with MoCo v3	1000	80	0.8708	4.7500	0.7790
Self-supervised Pretraining with MoCo v3	1000	160	0.9391	1.5000	0.8855
Self-supervised Pretraining with MoCo v3	2000	40	0.8857	3.0000	0.7959
Self-supervised Pretraining with MoCo v3	2000	80	0.9019	3.3268	0.8232
Self-supervised Pretraining with MoCo v3	2000	160	0.9415	1.2071	0.8898
Self-supervised Pretraining with MoCo v3	3000	40	0.8965	2.3090	0.8133
Self-supervised Pretraining with MoCo v3	3000	80	0.8854	2.5792	0.7969
Self-supervised Pretraining with MoCo v3	3000	160	0.9351	1.6036	0.8782
Self-supervised Pretraining with MAE	1000	40	0.8971	2.3090	0.8144
Self-supervised Pretraining with MAE	1000	80	0.9025	2.2500	0.8232
Self-supervised Pretraining with MAE	1000	160	0.9391	1.4571	0.8856
Self-supervised Pretraining with MAE	2000	40	0.8926	2.5000	0.8072
Self-supervised Pretraining with MAE	2000	80	0.9002	2.2500	0.8196
Self-supervised Pretraining with MAE	2000	160	0.9390	1.6036	0.8853
Self-supervised Pretraining with MAE	3000	40	0.8889	2.5590	0.8015
Self-supervised Pretraining with MAE	3000	80	0.8992	2.2500	0.8180
Self-supervised Pretraining with MAE	3000	160	0.9408	1.6036	0.8886
Task-agnostic KD (SAM)	1000	40	0.8719	4.0000	0.7752
Task-agnostic KD (SAM)	1000	80	0.8774	2.7500	0.7832
Task-agnostic KD (SAM)	1000	160	0.9163	2.0000	0.8458
Task-agnostic KD (SAM)	2000	40	0.8501	5.2932	0.7447
Task-agnostic KD (SAM)	2000	80	0.8716	3.9271	0.7742
Task-agnostic KD (SAM)	2000	160	0.9079	2.2071	0.8317
Task-agnostic KD (SAM)	3000	40	0.8659	3.8090	0.7673
Task-agnostic KD (SAM)	3000	80	0.8872	2.7500	0.7984
Task-agnostic KD (SAM)	3000	160	0.9019	2.7500	0.8215
Task-specific KD (SAM)	1000	40	0.8711	4.0207	0.7746
Task-specific KD (SAM)	1000	80	0.8908	2.7500	0.8043
Task-specific KD (SAM)	1000	160	0.9329	1.5000	0.8744
Task-specific KD (SAM)	2000	40	0.8655	4.0656	0.7650
Task-specific KD (SAM)	2000	80	0.8888	3.0000	0.8012
Task-specific KD (SAM)	2000	160	0.9373	1.5000	0.8823
Task-specific KD (SAM)	3000	40	0.8826	3.1920	0.7909
Task-specific KD (SAM)	3000	80	0.9075	2.0590	0.8314
Task-specific KD (SAM)	3000	160	0.9455	1.3536	0.8972

fine-tuning labels increase. Across most datasets, TSKD consistently achieves higher Dice scores,

with clear advantages observed as the transfer dataset size expands from 1000 to 3000 synthetic

Table 5: Segmentation performance comparison for DRIVE dataset across different methods, label counts, and transfer strategies.

Method Description	Transfer Data Scale	Number of Labels	Dice	HD95 (mm)	mIoU
Small ViT Model Initialized Randomly	-	5	0.2164	54.6548	0.1214
Small ViT Model Initialized Randomly	-	10	0.2076	55.5470	0.1159
Small ViT Model Initialized Randomly	-	20	0.3284	45.0434	0.1965
ImageNet Pre-trained Small ViT Model with MAE	-	5	0.2834	51.5239	0.1651
ImageNet Pre-trained Small ViT Model with MAE	-	10	0.2884	52.9268	0.1685
ImageNet Pre-trained Small ViT Model with MAE	-	20	0.3909	44.0781	0.2430
Self-supervised Pretraining with MoCo v3	1000	5	0.2283	54.2425	0.1289
Self-supervised Pretraining with MoCo v3	1000	10	0.2330	54.8677	0.1319
Self-supervised Pretraining with MoCo v3	1000	20	0.3352	45.2392	0.2014
Self-supervised Pretraining with MoCo v3	2000	5	0.2270	54.3608	0.1281
Self-supervised Pretraining with MoCo v3	2000	10	0.2269	55.0593	0.1280
Self-supervised Pretraining with MoCo v3	2000	20	0.3341	45.2834	0.2005
Self-supervised Pretraining with MoCo v3	3000	5	0.2327	53.8865	0.1317
Self-supervised Pretraining with MoCo v3	3000	10	0.2261	55.0819	0.1275
Self-supervised Pretraining with MoCo v3	3000	20	0.3378	45.0212	0.2033
Self-supervised Pretraining with MAE	1000	5	0.2578	51.7627	0.1480
Self-supervised Pretraining with MAE	1000	10	0.2437	54.8767	0.1388
Self-supervised Pretraining with MAE	1000	20	0.3607	44.5534	0.2201
Self-supervised Pretraining with MAE	2000	5	0.2623	52.0017	0.1510
Self-supervised Pretraining with MAE	2000	10	0.2681	53.9653	0.1549
Self-supervised Pretraining with MAE	2000	20	0.3678	44.4294	0.2253
Self-supervised Pretraining with MAE	3000	5	0.2665	51.5299	0.1537
Self-supervised Pretraining with MAE	3000	10	0.2722	53.6536	0.1576
Self-supervised Pretraining with MAE	3000	20	0.3689	44.2544	0.2262
Task-agnostic KD (SAM)	1000	5	0.1689	23.2676	0.0923
Task-agnostic KD (SAM)	1000	10	0.2134	7.7363	0.1195
Task-agnostic KD (SAM)	1000	20	0.4472	5.6081	0.2880
Task-agnostic KD (SAM)	2000	5	0.1540	13.6587	0.0834
Task-agnostic KD (SAM)	2000	10	0.2777	9.3260	0.1612
Task-agnostic KD (SAM)	2000	20	0.4097	8.6742	0.2576
Task-agnostic KD (SAM)	3000	5	0.1935	8.4051	0.1071
Task-agnostic KD (SAM)	3000	10	0.2324	8.9088	0.1315
Task-agnostic KD (SAM)	3000	20	0.4142	6.6469	0.2612
Task-specific KD (SAM)	1000	5	0.2207	5.5909	0.1241
Task-specific KD (SAM)	1000	10	0.3040	8.8596	0.1792
Task-specific KD (SAM)	1000	20	0.4940	5.4704	0.3280
Task-specific KD (SAM)	2000	5	0.2376	6.6997	0.1349
Task-specific KD (SAM)	2000	10	0.3873	5.2386	0.2402
Task-specific KD (SAM)	2000	20	0.5049	4.2361	0.3378
Task-specific KD (SAM)	3000	5	0.2886	4.3452	0.1687
Task-specific KD (SAM)	3000	10	0.4351	5.2881	0.2781
Task-specific KD (SAM)	3000	20	0.5741	3.8028	0.4026

images, and as the labeled sample count rises from minimal to full scale.

The qualitative results in Figure 4 further illustrate the impact of different pretraining strategies on the segmentation performance of a small Vision Transformer (ViT) model across diverse medical image datasets. Task-specific KD captures fine-grained anatomical details more accurately than other methods, which is essential for achieving high performance in medical segmentation tasks.

KidneyUS Dataset. The experimental results on the KidneyUS dataset (Table 1 and Figure 5) demonstrate the superiority of Task-Specific KD over other methods across varying transfer dataset sizes and labeled samples. Task-Specific KD achieved the highest mean Dice score of 0.6139 when using 3000 transfer images and 234 labeled examples, outperforming task-agnostic KD, MoCo v3, and MAE-based pretraining methods. For all segmentation regions—Capsule, Medulla, Central Echo Complex, and Cortex—Task-Specific KD consistently provided better Dice scores and HD95 metrics.

For instance, in the Medulla, Task-Specific KD achieved a Dice score of 0.7615, notably better than the corresponding scores of task-agnostic KD (Dice: 0.7104) and MAE (Dice: 0.7275). With fewer labeled examples (80 or 160), Task-Specific KD maintained a performance edge. For example, with 160 labeled examples and 1000 transfer images, it achieved a mean Dice score of 0.5615, compared to 0.5307 for task-agnostic KD and 0.5550 for MAE, emphasizing the robustness of Task-Specific KD across different data scales. Additionally, Task-Specific KD scaled more effectively with increasing transfer dataset sizes. Dice scores consistently improved with larger transfer datasets, rising from 0.4980 with 1000 images to 0.5616 with 3000 images (using 80 labeled samples during the fine-tuning phase), a trend less evident in other methods, which saw diminishing gains.

Autooral Dataset. The Task-Specific KD approach achieved the highest segmentation performance on the Autooral dataset, as depicted in Figure 6 and Table 2. With a Dice score of 0.5754 using 300 labeled examples and 3000

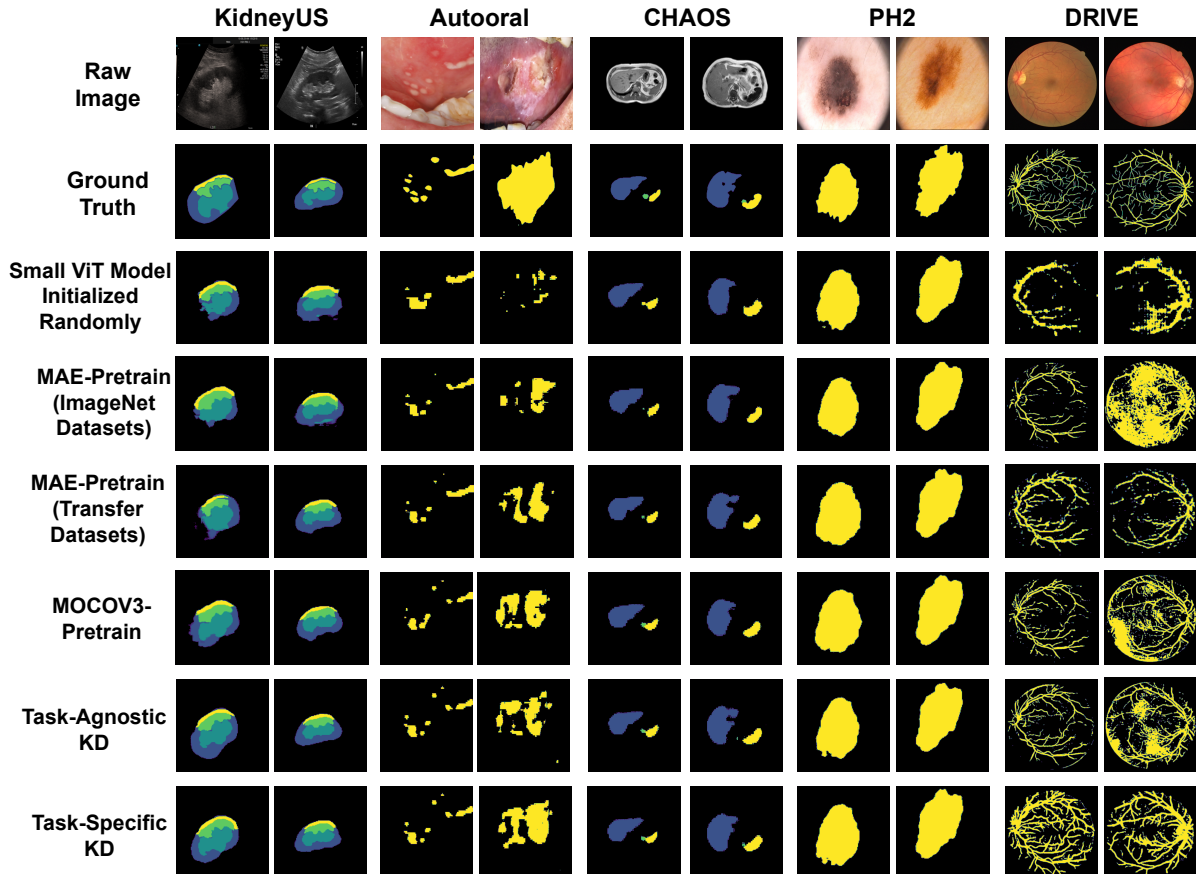


Fig. 4: Qualitative comparison of segmentation results for a small Vision Transformer (ViT) model fine-tuned using different pretraining strategies across five medical image datasets (KidneyUS, Autooral, CHAOS, PH2, and DRIVE). Rows represent various pretraining and knowledge distillation strategies: Random Initialization, MAE-Pretrain (ImageNet Datasets), MAE-Pretrain (Transfer Datasets), MOCOv3-Pretrain (Transfer Datasets), Task-Agnostic KD (Transfer Datasets), and Task-Specific KD (Transfer Datasets). Each column corresponds to a dataset, with segmentation results visualized for representative samples. Task-Specific KD consistently produces segmentations that are more accurate and closely aligned with ground truth, demonstrating its effectiveness in leveraging task-specific features in medical image segmentation.

transfer images, outperforming all other methods, including Task-Agnostic KD (Dice: 0.5688), MoCo v3 (Dice: 0.4636), and MAE (Dice: 0.5416). This demonstrates the advantage of task-specific KD in capturing domain-relevant features, particularly for ulcer segmentation. With 200 labeled examples, Task-Specific KD also showed superior results, scoring 0.5570, compared to 0.5109 for Task-Agnostic KD and 0.5112 for MAE. Even

with 100 labeled examples, it maintained a competitive Dice score of 0.3840, slightly outperforming MoCo v3 and MAE, showcasing robustness in data-limited settings. The performance of Task-Specific KD improved with larger transfer datasets, increasing from 0.5320 with 1000 transfer images to 0.5754 with 3000 transfer images (using 300 labeled samples during the fine-tuning phase), while other methods showed diminishing returns. Additionally, it demonstrated better boundary precision, with an HD95 of 9.57 mm, compared to Task-Agnostic KD (13.22 mm),

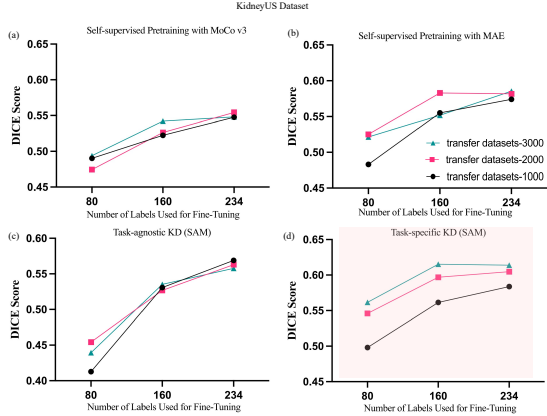


Fig. 5: Segmentation performance on the KidneyUS dataset across different pre-training and knowledge distillation methods. (a) Dice score trends for self-supervised pretraining with MoCo v3 using transfer datasets of varying sizes (1000, 2000, and 3000 images). (b) Dice score trends for self-supervised pretraining with MAE using different transfer dataset sizes. (c) Dice score trends for task-agnostic KD (SAM) across different transfer dataset sizes and numbers of labeled samples used for fine-tuning. (d) Dice score trends for task-specific KD (SAM) show superior performance across all labeled sample sizes and transfer dataset scales, demonstrating the most significant performance improvements when larger transfer datasets are used.

further highlighting its ability to capture fine anatomical details.

CHAOS Dataset. Task-Specific KD achieved the highest segmentation performance on the CHAOS dataset, with a Dice score of 0.8663 using 296 labeled samples, surpassing Task-Agnostic KD (0.8465) and other self-supervised methods (Table 3, Figure 7). Task-Specific KD excelled in segmenting complex organs, achieving superior Dice scores for the liver (0.8955), left kidney (0.8680), and spleen (0.8463), outperforming Task-Agnostic KD across these structures. Scalability was another strength: Task-specific KD improved with larger transfer datasets, with Dice scores rising from 0.8248 (1000 images) to 0.8663 (3000 images) when using 296 labeled samples. It also demonstrated better boundary precision, with a mean HD95 of 4.19 mm, outperforming Task-Agnostic KD (4.53 mm). Even with fewer labeled

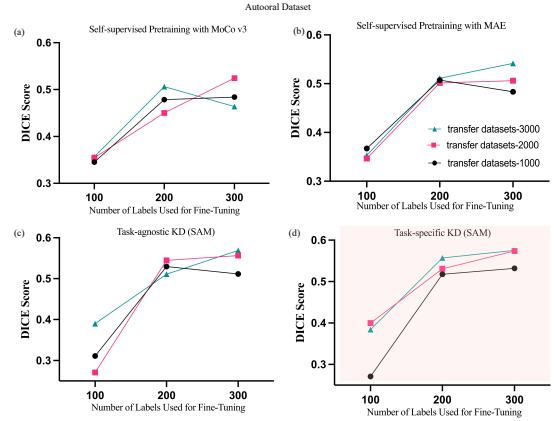


Fig. 6: Segmentation performance on the Autooral dataset using various pre-training and knowledge distillation methods. (a) Dice score comparison across different numbers of labeled samples (100, 200, 300) for self-supervised pretraining with MoCo v3 using transfer datasets of varying sizes (1000, 2000, and 3000 images). (b-d) Dice score trends for each method under varying transfer dataset sizes, with Task-Specific KD consistently showing superior performance, especially with 300 labeled examples.

samples (100 or 200), Task-Specific KD maintained its performance edge, delivering robust results in challenging segmentation tasks.

PH2 Dataset. For skin lesion segmentation on the PH2 dataset, Task-Specific KD demonstrated the most substantial performance boost, achieving a Dice score of 0.9455 with 160 labeled samples and a transfer dataset size of 3000, as seen in Figure 8 and Table 4. This score significantly exceeded the performance of models trained from scratch or using task-agnostic KD, indicating that leveraging domain-specific knowledge distillation is particularly beneficial in dermatological tasks where fine-grained lesion details are crucial for accurate diagnosis.

DRIVE Dataset. Our experiments on the DRIVE dataset, aimed at retinal vessel segmentation, showed that Task-Specific KD reached a Dice score of 0.5741, outperforming other pre-training methods, including self-supervised and task-agnostic KD, by a substantial margin. The model achieved the lowest HD95 value of 3.8028 mm, indicative of superior boundary delineation performance, as illustrated in Figure 9

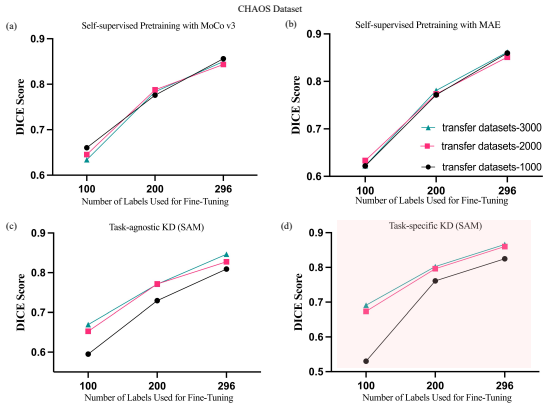


Fig. 7: Segmentation performance on the CHAOS dataset for various pre-training and knowledge distillation methods. (a) Dice score comparison across different numbers of labeled samples (100, 200, 296) for self-supervised pretraining with MoCo v3 using transfer datasets of varying sizes (1000, 2000, and 3000 images). (b-d) Detailed Dice score trends for MAE, task-agnostic KD, and task-specific KD across different transfer dataset scales, illustrating that Task-Specific KD consistently delivers superior performance, especially with increasing labeled samples and larger transfer datasets.

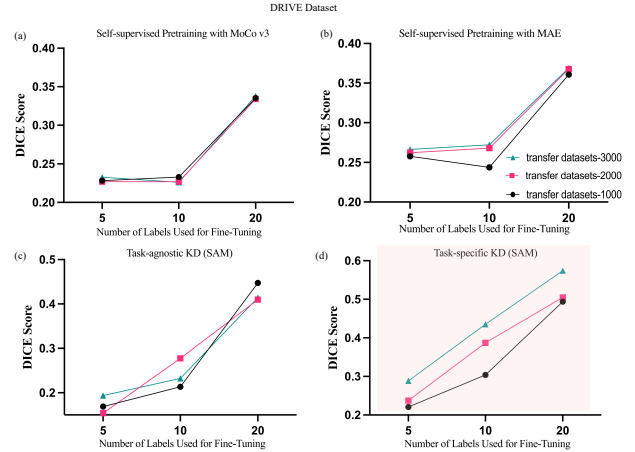


Fig. 9: Performance comparison on the DRIVE dataset for retinal vessel segmentation, highlighting the effectiveness of various pre-training and knowledge distillation methods. (a-d) Trends in Dice score for self-supervised pre-training (MoCo v3, MAE) and knowledge distillation methods, show that Task-Specific KD provides the most substantial performance improvement, especially with limited labeled data. Task-specific KD also demonstrated superior boundary delineation as reflected by its lowest HD95 value.

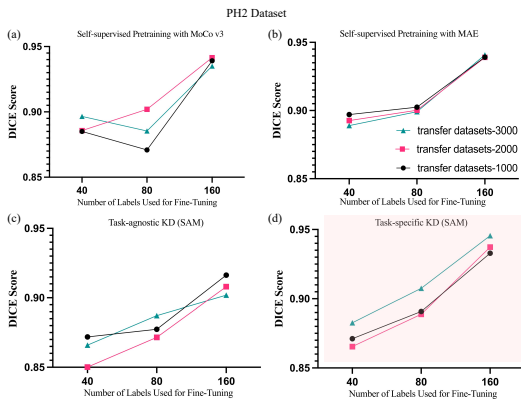


Fig. 8: Performance comparison of different methods on the PH2 dataset for skin lesion segmentation, measured in Dice score. (a-d) Detailed analysis of self-supervised approaches (MoCo v3 and MAE) and knowledge distillation (task-agnostic and task-specific KD) across varying transfer dataset scales.

and Table 5. The ability to maintain high accuracy in vessel segmentation, even with limited labeled data, underscores the capability of our Task-Specific KD framework to effectively transfer detailed semantic information, which is crucial for vascular structure analysis.

Comparison Across Datasets. Across all datasets, Task-Specific KD demonstrated superior performance, particularly in low-data regimes where data scarcity is most problematic. The consistent improvements in Dice, HD95, and mean Intersection over Union (mIoU) metrics emphasize the importance of tailoring pre-trained VFM to specific target tasks. The domain-specific adaptation facilitated by LoRA fine-tuning played a crucial role in enhancing the segmentation performance of our student model, thereby supporting efficient deployment without compromising accuracy.

The experimental results underscore the efficacy of Task-Specific KD combined with LoRA fine-tuning in significantly boosting segmentation performance across diverse medical imaging tasks.

By effectively leveraging the domain-specific knowledge captured by VFM, our approach provides a robust solution for specific medical image segmentation, demonstrating its potential for broader application in clinical practice.

4.3.2 Importance of Transfer Set Size

The size of the transfer dataset plays a crucial role in the performance of pre-training strategies for medical image segmentation, with our experiments highlighting three key insights. First, larger transfer sets resulted in improved segmentation performance across different methods and datasets. For instance, in the DRIVE dataset, Task-Specific KD with 3000 transfer images and 20 fine-tuning labels achieved a 16.22% improvement in the Dice score compared to using 1000 transfer images. Similarly, in the KidneyUS dataset, Task-Specific KD achieved a Dice score of 0.6139 using 3000 transfer images and 234 fine-tuning labels, compared to 0.5837 with 1000 transfer images. These results underscore the importance of larger transfer sets in learning robust feature representations, especially for complex segmentation tasks such as retinal vessel and kidney images.

However, we also observed diminishing returns beyond a certain dataset size. For example, in the Autooral dataset, the Dice score improvement from 2000 to 3000 transfer images was significantly smaller than the leap from 1000 to 2000 images. This suggests that while expanding transfer dataset size can enhance performance, the gains eventually plateau as the model reaches its optimal learning capacity, indicating the need for a practical balance between dataset size and computational cost. Interestingly, knowledge distillation methods, particularly Task-Specific KD, demonstrated notable efficiency even with smaller transfer sets. In the PH2 dataset, Task-Specific KD achieved a Dice score of 0.9329 with just 1000 transfer images (160 fine-tuning labels), which was close to the performance of 0.9455 achieved with 3000 images. This indicates that leveraging knowledge distillation from a fine-tuned large model, such as SAM, can effectively bridge the gap in data-scarce scenarios, making it a powerful strategy for medical applications where labeled data is often limited.

4.3.3 Training Efficiency

In this section, we compare the training efficiency and segmentation performance across five medical imaging datasets using various pre-training strategies. The methods evaluated include MAE pre-trained on ImageNet, MAE pre-trained on transfer datasets, MoCo v3 pre-training, Task-Agnostic Knowledge Distillation (KD), and Task-Specific KD. The experimental results, along with GPU training times, are detailed in Table 6.

Pre-training on ImageNet (MAE).

For the MAE pre-training on ImageNet, we utilized pre-trained weights and training times as reported [51]. Specifically, the MAE model was trained for 400 epochs on ImageNet using a system equipped with 8 NVIDIA V100 GPUs, which required approximately 23 hours. Subsequently, the model was fine-tuned for each medical imaging task using the maximum number of labeled samples available. Despite yielding competitive performance, this approach required substantial computational resources due to the extensive ImageNet pre-training.

Pre-training on Transfer Datasets.

For the remaining methods—MAE pre-trained on transfer datasets, MoCo v3 pre-training, Task-Agnostic KD, and Task-Specific KD—we employed synthetic transfer datasets generated using a Swin-transformer-based diffusion model. These pre-training processes were executed on two NVIDIA L40 GPUs for 1600 epochs across all methods. The pre-training times varied based on the complexity of the strategy, with Task-Specific KD requiring slightly longer due to the additional task-specific knowledge distillation step.

Comparison of Pre-training Methods.

The Task-Specific KD approach consistently achieved the best segmentation performance across all datasets, demonstrating substantial improvements, particularly in challenging tasks such as retinal vessel segmentation (DRIVE dataset), where it delivered a 74.82% improvement. This significant gain can be attributed to the fine-tuning of the SAM model on each specific medical imaging task before knowledge distillation, thereby optimizing both the encoder and decoder for the target task. The task-specific

Table 6: Comparison of pre-training methods and GPU hours on segmentation performance across multiple medical datasets.

Target Task	Method	GPU Hours (Pre-training)	Performance (Mean Dice)	Performance Improvement (%)
kidneyus	MAE-Pretrain (ImageNet Datasets)	23h*	0.5449	0.8254
	MAE-Pretrain (Transfer Datasets)	2.5h	0.5855	8.3315
	MOCOv3-Pretrain (Transfer Datasets)	30.6h	0.5481	1.4166
	Task-Agnostic KD (Transfer Datasets)	16h	0.5577	3.1902
	Task-Specific KD (Transfer Datasets)	16.2h	0.6139	13.5861
Autooral	MAE-Pretrain (ImageNet Datasets)	23h*	0.5495	22.9364
	MAE-Pretrain (Transfer Datasets)	0.9h	0.5416	21.1611
	MOCOv3-Pretrain (Transfer Datasets)	3.6h	0.4636	3.7003
	Task-Agnostic KD (Transfer Datasets)	2.8h	0.5688	27.2459
	Task-Specific KD (Transfer Datasets)	3h	0.5754	28.7239
Chaos	MAE-Pretrain (ImageNet Datasets)	23h*	0.8582	5.7740
	MAE-Pretrain (Transfer Datasets)	0.9h	0.8616	6.1863
	MOCOv3-Pretrain (Transfer Datasets)	3.6h	0.8498	4.7356
	Task-Agnostic KD (Transfer Datasets)	2.8h	0.8465	4.3269
	Task-Specific KD (Transfer Datasets)	3h	0.8663	6.7628
PH2	MAE-Pretrain (ImageNet Datasets)	23h*	0.9266	0.9861
	MAE-Pretrain (Transfer Datasets)	2.5h	0.9408	2.5329
	MOCOv3-Pretrain (Transfer Datasets)	30.6h	0.9351	1.9073
	Task-Agnostic KD (Transfer Datasets)	16h	0.9019	-1.7093
	Task-Specific KD (Transfer Datasets)	16.2h	0.9455	3.0466
DRIVE	MAE-Pretrain (ImageNet Datasets)	23h*	0.3909	19.0395
	MAE-Pretrain (Transfer Datasets)	2.5h	0.3689	12.3298
	MOCOv3-Pretrain (Transfer Datasets)	30.6h	0.3378	2.8792
	Task-Agnostic KD (Transfer Datasets)	16h	0.4142	26.1234
	Task-Specific KD (Transfer Datasets)	16.2h	0.5741	74.8218

fine-tuning allowed the student model to benefit from more specialized feature representations and segmentation outputs, leading to superior performance.

Conversely, the Task-Agnostic KD method, which aligns only the encoder representations, demonstrated comparatively lower performance. This method relied on the original, unmodified SAM encoder without task-specific fine-tuning, resulting in less effective transfer of knowledge to the student model. In tasks requiring detailed and fine-grained segmentation, such as retinal vessel extraction, the relevance of the knowledge transferred was notably reduced. These findings emphasize the importance of fine-tuning large models such as SAM on the target domain before distillation, as this significantly enhances the relevance and utility of the transferred knowledge.

GPU Training Time Analysis.

The MAE pre-training on ImageNet was the most computationally demanding, with a pre-training time of 23 hours. In contrast, methods utilizing transfer datasets required significantly less time, with the shortest pre-training time recorded at 0.9 hours for the Autooral dataset. Task-Specific KD required 16.2 hours of pre-training, making it more computationally intensive compared to other transfer dataset methods, but still considerably more efficient than ImageNet-based pre-training.

MoCo v3 pre-training, while competitive in certain tasks, exhibited the longest pre-training time among the transfer dataset methods at 30.6 hours, likely due to the larger batch size and the complexity of the contrastive learning objective.

Performance and Computational Trade-offs.

Despite the computational overhead of Task-Specific KD, the associated performance gains justified the additional pre-training time. Compared to the MAE pre-training on ImageNet, Task-Specific KD achieved superior performance on most datasets while requiring significantly less pre-training time. This efficiency, combined with its ability to transfer task-specific knowledge effectively, positions it as a promising alternative to traditional large-scale pre-training approaches. As summarized in Table 6, Task-Specific KD consistently delivered the best performance improvements, particularly in challenging segmentation tasks such as retinal vessel segmentation (DRIVE dataset) and kidney ultrasound (KidneyUS dataset), where capturing intricate details is critical. These results underscore the potential of Task-Specific KD to achieve state-of-the-art segmentation performance while reducing computational demands.

4.3.4 Memory Efficiency and Performance of ViT-Tiny

One of the key advantages of Task-Specific Knowledge Distillation (KD) is the ability to compress large models, like SAM, into smaller models, such as ViT-Tiny, without significant loss in segmentation performance. Table 7 compares the memory footprint and segmentation accuracy (Dice scores) of the SAM-LoRA model, fine-tuned with the smallest labeled dataset, and the ViT-Tiny model was pre-trained using Task-Specific Knowledge Distillation (TSKD) on a transfer dataset consisting of 3000 synthetic images, followed by fine-tuning with the minimum number of labeled samples available for each dataset.

The results in Table 7 demonstrate that ViT-Tiny, trained using Task-Specific KD, offers significant memory savings while achieving competitive segmentation performance. With only 33 MB of memory, ViT-Tiny achieves Dice scores close to, and sometimes even surpasses, the much larger SAM-LoRA model. For example, in the CHAOS dataset, ViT-Tiny slightly outperformed SAM-LoRA, achieving a Dice score of 0.6912 compared to SAM-LoRA’s 0.6799, while consuming nearly ten times less memory.

In the PH2 dataset, which involves skin lesion segmentation, ViT-Tiny achieved a Dice score of 0.8826, almost identical to SAM-LoRA’s 0.8786, further highlighting the effectiveness of KD in transferring task-specific knowledge from a large teacher model to a small student model without sacrificing segmentation accuracy.

For more complex datasets such as Autooral and DRIVE, where anatomical details or fine structures are more challenging to segment, SAM-LoRA’s higher capacity led to noticeably better performance. For instance, in the Autooral dataset, SAM-LoRA achieved a Dice score of 0.7056, significantly higher than ViT-Tiny’s 0.3840. This suggests that while ViT-Tiny is highly memory-efficient, it may struggle with more intricate segmentation tasks when compared to its larger counterpart.

Despite these trade-offs, Task-Specific KD enables ViT-Tiny to achieve competitive performance with minimal memory usage, making it a strong candidate for resource-limited applications in medical image analysis.

4.4 Ablation Study

4.4.1 Impact of Task-Specific KD Loss Weights

The results of our experiments on task-specific knowledge distillation (KD) demonstrate the effectiveness of fine-tuning the SAM model and transferring its domain-specific knowledge to a smaller Vision Transformer (ViT) model for medical image segmentation tasks. By leveraging both MSE and Hidden States distillation losses, we achieved notable improvements in segmentation accuracy across various anatomical structures within the CHAOS dataset, as detailed in Table 8 and Table 9.

In particular, the experiment group **TS-KD8**, which employed a higher MSE weight of 0.2 alongside a moderate Hidden Loss weight of 0.1, achieved the best overall performance, with a mean Dice score of **0.8663** and an HD95 of **4.19 mm**. This configuration balanced the contributions of spatial alignment and feature representation transfer, proving especially effective for segmenting complex anatomical structures like the liver and kidneys. For instance, in the case of the left kidney, **TS-KD8** achieved a Dice score of **0.8680** with an HD95 of **1.37 mm**, outperforming other configurations in terms of both segmentation accuracy and boundary precision.

Comparatively, the lower MSE weight in **TS-KD7** (MSE: 0.1, Hidden Loss: 0.1) resulted in a slightly reduced Dice score of 0.8450, with an HD95 of 4.63mm. This suggests that while moderate MSE weighting helps maintain reasonable segmentation quality, increasing the MSE weight yields more precise spatial alignment, especially in structures with intricate boundaries, such as the spleen, where TS-KD8 recorded a Dice score of 0.8463 compared to 0.8021 in TS-KD7.

The role of Hidden States distillation was further highlighted by the comparison with TS-KD6, which did not employ Hidden Loss and relied solely on MSE. This configuration, although achieving a competitive Dice score of 0.8461, lagged in boundary precision with an HD95 of 4.37mm. The absence of Hidden Loss in TS-KD6 likely reduced the model’s ability to transfer rich feature representations from the teacher to the student, resulting in slightly inferior performance, especially in structures like the right kidney, where

Table 7: Comparison of memory and segmentation performance across different datasets for SAM-LoRA (fine-tuned on the smallest labeled dataset) and ViT-Tiny (trained with Task-Specific KD). ViT-Tiny was trained using a transfer dataset of 3000 synthetic images and fine-tuned with the smallest labeled dataset.

Dataset	SAM Size (MB)	LoRA SAM Extra Memory (MB)	ViT-Tiny + Seg Head (MB)	SAM-LoRA Dice (Small Label Set)	ViT-Tiny Dice (Task-Specific KD)
KidneyUS	357	17.2	33.5	0.5499	0.5616
Autooral	357	15.3	33.0	0.7056	0.3840
CHAOS	357	18.8	33.0	0.6799	0.6912
PH2	357	16.1	33.5	0.8786	0.8826
DRIVE	357	16.1	33.5	0.7083	0.2886

Table 8: Summary of KD loss functions, mask processing, and loss weights in task-specific KD experiments. Each experiment typically includes two types of KD: (1) KD applied at the decoder level, focusing on aligning segmentation outputs (e.g., using MSE or CrossEntropy for spatial alignment of masks); and (2) KD applied at the encoder level, where hidden states from the teacher and student models are aligned to transfer rich feature representations. However, in TS-KD6, only decoder-level KD (MSE) is applied, with no hidden states distillation. The table also details how SAM’s low-resolution logits were processed (interpolated or uninterpolated) and specifies the loss weights assigned to each KD term, balancing the contributions of spatial alignment and feature representation transfer.

Experiment Group	Loss Type	Mask Processing	Hidden States Distillation	Loss Weights	Features
TS-KD1	MSE + Hidden Loss	Removing the last dimension of masks	Yes	MSE weight: 0.2 Hidden Loss weight: 1.0	Emphasizes Hidden States alignment; MSE for mask alignment
TS-KD2	MSE + Hidden Loss	Low-res logits interpolated to student output size	Yes	MSE weight: 0.1 Hidden Loss weight: 1.0	Aligns low-res logits, reduces high-res dependency
TS-KD3	MSE + Hidden Loss	Uninterpolated low-res logits	Yes	MSE weight: 0.001 Hidden Loss weight: 1.0	Removes interpolation, low-weight MSE loss
TS-KD4	CrossEntropy + Hidden Loss	CrossEntropy loss aligns class probability distribution	Yes	CrossEntropy weight: 1.0 Hidden Loss weight: 1.0	Focuses on class alignment, using CrossEntropy instead of MSE
TS-KD5	CrossEntropy + Hidden Loss	CrossEntropy loss aligns class probability distribution	Yes, reduced weight	CrossEntropy weight: 1.0 Hidden Loss weight: 0.1	Similar to TS-KD4 but with reduced Hidden States weight
TS-KD6	MSE	Interpolated low-res logits	No	MSE weight: 0.1 Hidden Loss weight: 0.0	No Hidden Loss, focuses on MSE loss
TS-KD7	MSE + Hidden Loss	Interpolated low-res logits	Yes	MSE weight: 0.1 Hidden Loss weight: 0.1	Restores interpolation, moderate MSE alignment
TS-KD8	MSE + Hidden Loss	Interpolated low-res logits	Yes	MSE weight: 0.2 Hidden Loss weight: 0.1	Similar to TS-KD7 but with increased MSE loss weight

Table 9: Segmentation performance (Dice score and HD95) across different organs in the CHAOS dataset for various task-specific KD configurations (TS-KD1 to TS-KD8). The experiments utilize a training dataset that includes 3000 synthetic images for pre-training and 296 labeled real images for fine-tuning.

Method Description	Transfer Data Scale	Number of Labels	Liver		Right kidney		Left kidney		Spleen		Mean	
			Dice	HD95 (mm)	Dice	HD95 (mm)	Dice	HD95 (mm)	Dice	HD95 (mm)	Dice	HD95 (mm)
TS-KD1	3000	296	0.8808	2.5128	0.8111	15.6951	0.8292	3.2780	0.7895	2.9886	0.8276	6.1186
TS-KD2	3000	296	0.8941	1.8926	0.8460	15.6645	0.8454	2.7490	0.7978	3.0528	0.8458	5.8397
TS-KD3	3000	296	0.8936	2.0968	0.8563	11.7962	0.8324	2.6420	0.7738	2.9762	0.8390	4.8778
TS-KD4	3000	296	0.8951	1.9194	0.8405	11.8118	0.8312	2.2376	0.7925	4.3790	0.8398	5.0869
TS-KD5	3000	296	0.8984	1.8240	0.8738	16.7558	0.8738	1.4999	0.8185	2.0363	0.8661	5.5290
TS-KD6	3000	296	0.8931	1.8755	0.8272	11.1423	0.8436	2.0077	0.8204	2.4476	0.8461	4.3683
TS-KD7	3000	296	0.8945	1.8026	0.8311	11.3921	0.8523	2.6433	0.8021	2.7018	0.8450	4.6350
TS-KD8	3000	296	0.8955	2.0779	0.8553	11.8028	0.8680	1.3695	0.8463	1.4954	0.8663	4.1864

TS-KD6 recorded an HD95 of $11.14mm$, compared to $11.80mm$ in TS-KD8.

In experiments utilizing CrossEntropy loss (TS-KD4 and TS-KD5), the results indicate that CrossEntropy is less effective than MSE in this task-specific KD framework. Although TS-KD5, with reduced Hidden Loss weight (0.1), achieved a respectable Dice score of 0.8661, it recorded an HD95 of $5.53mm$, indicating that it struggled to maintain precise boundary delineation, particularly for the right kidney, which had an HD95 of $16.76mm$. This finding supports the hypothesis that CrossEntropy, while effective in aligning class

probabilities, is less suited to the fine-grained spatial alignment required for medical segmentation tasks, particularly in the CHAOS dataset.

The interpolation of SAM’s low-resolution logits to match the student model’s output size proved to be an essential technique for transferring useful knowledge from the teacher model. In TS-KD8, this interpolation, coupled with the MSE loss, allowed the student model to better capture the spatial characteristics of the target structures, leading to improved segmentation performance. For example, in the liver, TS-KD8 achieved a Dice score of 0.8955 and an HD95 of $2.08mm$, compared

to 0.8808 and 2.51mm, respectively, in TS-KD1, which used a simpler mask processing approach.

Furthermore, the experiments revealed diminishing returns when reducing the MSE weight excessively. TS-KD3, with an MSE weight of 0.001, produced a Dice score of 0.8390 and an HD95 of 4.88mm, showing that an overly small MSE contribution undermines spatial alignment. This was evident in smaller structures like the spleen, where TS-KD3 recorded a Dice score of 0.7738, compared to 0.8463 in TS-KD8.

These results underscore the importance of balancing MSE and Hidden Loss in the KD framework. The configuration in **TS-KD8**, with its higher MSE weight, proved optimal for transferring spatial alignment and feature representations from the fine-tuned SAM model to the student ViT model. This combination of losses enabled the model to achieve superior segmentation accuracy and boundary precision, particularly in challenging structures within the CHAOS dataset. Task-specific KD, when fine-tuned with appropriately weighted losses, demonstrates substantial promise for improving medical image segmentation in data-limited scenarios.

4.4.2 LoRA rank Impact of SAM Model Fine-tuning

To investigate the influence of different LoRA ranks on the fine-tuning of the SAM model, we conducted experiments across a variety of datasets, employing a range of LoRA ranks. Our objective was to identify a LoRA rank that strikes an optimal balance between segmentation performance and model efficiency, which would later serve as the foundation for task-specific knowledge distillation (KD). Figure 10 presents the segmentation performance of the SAM model at various LoRA ranks, evaluated using the Dice score on datasets such as KidneyUS, Autooral, CHAOS, PH2, and DRIVE.

LoRA Rank Selection and Performance.

The experiments highlight that LoRA rank selection significantly affects the fine-tuning performance of the SAM model (as shown in Figure 10 and Table 10). Detailed results can be found in Appendix Tables 11–15:

- **KidneyUS Dataset (Figure 10a).** The results reveal a steady improvement in the Dice score with increasing LoRA rank, reaching a peak at rank 128. However, for subsequent experiments, a lower rank (Rank 4) was selected to achieve a competitive performance (0.6254 Dice score with 234 labels) while enhancing computational efficiency.
- **Autooral Dataset (Figure 10b).** A LoRA rank of 2 delivered strong segmentation performance, achieving a Dice score of 0.7056 with only 100 labeled images. This rank was subsequently chosen for KD experiments due to its minimal parameter overhead and reasonable accuracy.
- **CHAOS Dataset (Figure 10c).** Rank 16 was selected based on its significant enhancement in Dice score (up to 0.8651 with 296 labels), coupled with maintaining a moderate model size. This balance made it a suitable candidate for subsequent fine-tuning and KD tasks.
- **PH2 Dataset (Figure 10d).** A LoRA rank of 8 provided high segmentation accuracy (0.9677 Dice score with 160 labels), making it optimal for downstream KD tasks given its efficiency and robust performance.
- **DRIVE Dataset (Figure 10e).** Rank 8 was employed for fine-tuning using only 20 labels, yielding a Dice score of 0.7598. This rank was deemed suitable for subsequent KD experiments, ensuring efficiency while maintaining a high level of segmentation performance.

LoRA Rank Efficiency and Task-Specific SAM Fine-tuning.

Following the LoRA rank experiments, the selected ranks were used to fine-tune the SAM model with minimal labeled data for each task, thus serving as a task-specific SAM Teacher in the knowledge distillation framework (as shown in Table 10). For instance, in the DRIVE dataset, Rank 8 was chosen due to its efficiency in achieving strong segmentation with fewer parameters, providing an optimal balance for KD experiments.

The LoRA rank experiments allowed us to identify configurations that maximized segmentation performance while minimizing computational requirements. These fine-tuned models were subsequently employed as task-specific teachers within our knowledge distillation framework,

Table 10: Segmentation performance for selected LoRA ranks across different datasets and label counts.

Target Task	Lora rank	Number of Labels	Mean Dice	Mean HD95 (mm)
SAM&Lora Fine-Tuning (kidneyUS)	4	80	0.5499	12.7257
	4	160	0.6015	12.6120
	4	234	0.6254	13.2910
SAM&Lora Fine-Tuning (Autooral)	2	100	0.7056	19.9173
	2	200	0.7945	5.2674
	2	300	0.8121	4.1861
SAM&Lora Fine-Tuning (Chaos)	16	100	0.6799	14.2112
	16	200	0.7976	5.4063
	16	296	0.8651	2.9372
SAM&Lora Fine-Tuning (PH2)	8	40	0.8786	19.0440
	8	80	0.8984	17.4346
	8	160	0.9677	0.5000
SAM&Lora Fine-Tuning (DRIVE)	8	5	0.7083	2.9142
	8	10	0.7119	3.0000
	8	20	0.7598	2.1180

ensuring that student models received guidance from highly optimized, task-specific teachers. This methodology facilitated an efficient and effective transfer of knowledge, ultimately enhancing the performance of the overall segmentation framework. For more detailed experimental results of different rank Lora fine-tuning, see Table 11-Table15.

4.5 Effectiveness of Diffusion-Based Synthetic Transfer Data

To evaluate the quality of synthetic transfer datasets generated using diffusion models, we assessed the generated images compared to the original datasets using Peak Signal-to-Noise Ratio (PSNR) and Mean Squared Error (MSE) metrics. The evaluation, presented in Table 16, covered a range of medical imaging tasks, including KidneyUS, Autooral, CHAOS, PH2, and DRIVE. PSNR and MSE are standard metrics for assessing image quality, where higher PSNR values denote better image quality, and lower MSE values indicate closer similarity to the original images. Across all datasets, the diffusion model generated high-quality images, with PSNR values consistently around 27-28 dB and MSE values in the range of 104-111. This confirms that the generated images are visually similar to the original data, indicating that the synthetic datasets can serve as effective transfer sets for subsequent pre-training and fine-tuning tasks.

Notably, there was relatively little variation in the PSNR and MSE values across different datasets, suggesting that the diffusion model

maintained a high and consistent quality of generated images regardless of the medical imaging task. For instance, the Autooral Transfer dataset achieved a PSNR of 27.91 dB and an MSE of 105.26, while the DRIVE Transfer dataset achieved similar results, with a PSNR of 27.95 dB and an MSE of 104.41. This consistency across diverse medical imaging modalities, such as ultrasound, retinal fundus, and dermoscopic images, demonstrates the generalizability of the diffusion model in generating reliable synthetic data for various medical segmentation tasks. The high PSNR and low MSE values validate the generated datasets' suitability for use in transfer learning, particularly in scenarios with limited labeled data. By utilizing these synthetic datasets for pre-training, the models benefited from enhanced performance through knowledge distillation and fine-tuning, ensuring that the synthetic data effectively captured the structural and visual features necessary for medical image segmentation tasks. Overall, the results affirm that the diffusion model can generate high-quality synthetic datasets suitable for addressing data scarcity in medical imaging tasks by augmenting original datasets with visually consistent synthetic images.

5 Discussion and Conclusion

The results of our study highlight the effectiveness of task-specific knowledge distillation (KD) [16] and synthetic data generation for enhancing the performance of lightweight ViT models (such as ViT-Tiny) in medical image segmentation tasks. By utilizing a fine-tuned Vision Foundation Model

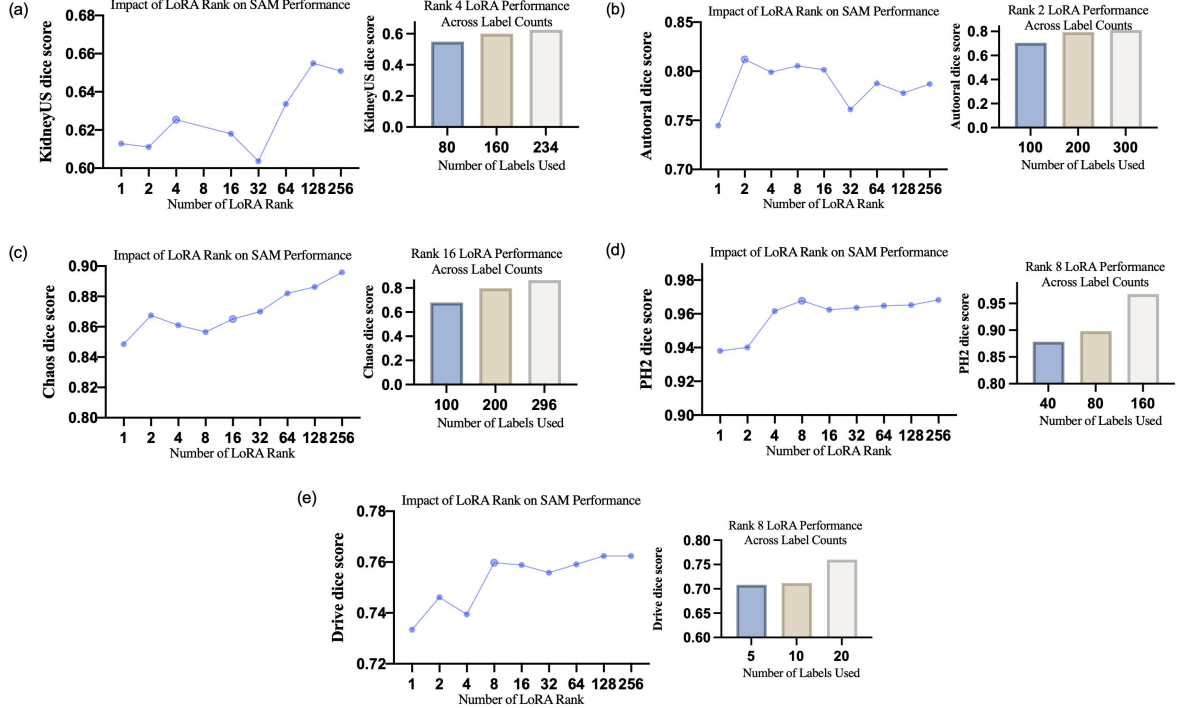


Fig. 10: Influence of LoRA rank on SAM model segmentation performance across five datasets (KidneyUS, Autooral, CHAOS, PH2, and DRIVE). Each subfigure shows: (1) Left: Line plots displaying Dice scores as LoRA rank varies, illustrating how changes in rank affect segmentation accuracy per dataset. Datasets like CHAOS and PH2 benefit from higher ranks, while Autooral achieves optimal results with lower ranks. (2) Right: Bar charts showing Dice scores at the selected LoRA rank across different labeled sample sizes for each dataset. These results guided the selection of efficient LoRA ranks for task-specific SAM fine-tuning, later applied in knowledge distillation (KD) with SAM as the teacher model.

Table 11: Effect of LoRA Rank on segmentation performance for SAM & LoRA Fine-Tuning on kidneyUS dataset with maximum labels.

Methods	Lora rank	Capsule		Medulla		Central Echo Complex		Cortex		Mean	
		Dice	HD95 (mm)	Dice	HD95 (mm)	Dice	HD95 (mm)	Dice	HD95 (mm)	Dice	HD95 (mm)
SAM&Lora Fine-Tuning	1	0.5557	6.0039	0.7585	6.5106	0.6157	17.2670	0.5216	35.4035	0.6129	16.2962
SAM&Lora Fine-Tuning	2	0.5220	6.7404	0.7704	5.0215	0.6212	11.1875	0.5306	32.1949	0.6111	13.7861
SAM&Lora Fine-Tuning	4	0.5601	5.6745	0.7693	6.3744	0.6234	13.9841	0.5487	27.1310	0.6254	13.2910
SAM&Lora Fine-Tuning	8	0.5324	5.2731	0.7560	4.9110	0.5965	17.6472	0.4941	44.0545	0.5948	17.9714
SAM&Lora Fine-Tuning	16	0.5572	5.1924	0.7757	4.2246	0.6144	15.8491	0.5250	41.8807	0.6181	16.7867
SAM&Lora Fine-Tuning	32	0.5248	5.2625	0.7679	5.5591	0.6157	16.7684	0.5064	24.2872	0.6037	12.9693
SAM&Lora Fine-Tuning	64	0.5660	5.7795	0.7655	4.9086	0.6575	7.2263	0.5455	22.5304	0.6337	10.1112
SAM&Lora Fine-Tuning	128	0.5896	4.6997	0.7971	3.9856	0.6603	11.5529	0.5729	26.2052	0.6550	11.6109
SAM&Lora Fine-Tuning	256	0.5980	4.7190	0.7921	4.2502	0.6708	13.2024	0.5426	23.7446	0.6509	11.4791

(VFM) as a teacher, we successfully transferred domain-specific knowledge to a smaller Vision Transformer (ViT) model, leading to consistent performance gains across diverse datasets, especially in data-limited scenarios. This was particularly evident in challenging cases like retinal vessel and skin lesion segmentation, where the fine-tuned SAM model provided critical insights

that enhanced the student’s ability to capture fine-grained structures.

Our dual-level distillation strategy, aligning both encoder representations and decoder output logits, effectively facilitated the transfer of robust feature representations and semantic priors. This proved invaluable in overcoming the challenges associated with limited labeled data, where high-quality annotations are costly and

Table 12: Effect of LoRA Rank on segmentation performance for SAM & LoRA Fine-Tuning on Autooral dataset with maximum labels.

Methods	Lora rank	Dice	HD95 (mm)	mIou
SAM&Lora Fine-Tuning	1	0.7446	6.9965	0.5982
SAM&Lora Fine-Tuning	2	0.8121	4.1861	0.6871
SAM&Lora Fine-Tuning	4	0.7991	4.7500	0.6688
SAM&Lora Fine-Tuning	8	0.8056	4.5794	0.6765
SAM&Lora Fine-Tuning	16	0.8016	5.4028	0.6729
SAM&Lora Fine-Tuning	32	0.7611	5.9271	0.6243
SAM&Lora Fine-Tuning	64	0.7877	6.7362	0.6527
SAM&Lora Fine-Tuning	128	0.7777	6.3947	0.6455
SAM&Lora Fine-Tuning	256	0.7870	5.6956	0.6521

Table 13: Effect of LoRA Rank on segmentation performance for SAM & LoRA Fine-Tuning on Chaos dataset with maximum labels.

Methods	Lora rank	Liver		Right kidney		Left kidney		Spleen		Mean	
		Dice	HD95 (mm)								
SAM&Lora Fine-Tuning	1	0.8864	1.7464	0.8563	8.8360	0.8255	2.0171	0.8258	2.3003	0.8485	3.7250
SAM&Lora Fine-Tuning	2	0.8921	1.9747	0.8713	16.2933	0.8612	1.7760	0.8453	2.0550	0.8675	5.5247
SAM&Lora Fine-Tuning	4	0.8935	1.6376	0.8461	9.3126	0.8530	3.4462	0.8515	2.0387	0.8610	4.1088
SAM&Lora Fine-Tuning	8	0.8954	1.5707	0.8520	11.5874	0.8432	2.3865	0.8355	3.9375	0.8565	4.8706
SAM&Lora Fine-Tuning	16	0.8902	1.7505	0.8555	4.9266	0.8751	1.6260	0.8397	3.4457	0.8651	2.9372
SAM&Lora Fine-Tuning	32	0.8889	1.8293	0.8720	11.4989	0.8788	1.5013	0.8405	2.5422	0.8701	4.3429
SAM&Lora Fine-Tuning	64	0.8962	1.6844	0.8717	11.6787	0.8842	1.8182	0.8759	1.8611	0.8820	4.2606
SAM&Lora Fine-Tuning	128	0.9093	1.3769	0.8844	8.6901	0.8846	1.4906	0.8667	1.9378	0.8863	3.3739
SAM&Lora Fine-Tuning	256	0.9123	1.4228	0.8980	11.3756	0.8991	1.4766	0.8743	1.3869	0.8959	3.9155

Table 14: Effect of LoRA Rank on segmentation performance for SAM & LoRA Fine-Tuning on PH2 dataset with maximum labels.

Methods	Lora rank	Dice	HD95 (mm)	mIou
SAM&Lora Fine-Tuning	1	0.9381	1.9014	0.8852
SAM&Lora Fine-Tuning	2	0.9401	1.2071	0.8888
SAM&Lora Fine-Tuning	4	0.9616	0.7500	0.9262
SAM&Lora Fine-Tuning	8	0.9677	0.5000	0.9375
SAM&Lora Fine-Tuning	16	0.9624	0.7500	0.9277
SAM&Lora Fine-Tuning	32	0.9636	0.6036	0.9299
SAM&Lora Fine-Tuning	64	0.9648	0.5000	0.9321
SAM&Lora Fine-Tuning	128	0.9652	0.5000	0.9328
SAM&Lora Fine-Tuning	256	0.9682	0.2500	0.9385

Table 15: Effect of LoRA Rank on segmentation performance for SAM & LoRA Fine-Tuning on DRIVE dataset with maximum labels.

Methods	Lora rank	Dice	HD95 (mm)	mIou
SAM&Lora Fine-Tuning	1	0.7334	2.5322	0.5790
SAM&Lora Fine-Tuning	2	0.7462	2.2247	0.5952
SAM&Lora Fine-Tuning	4	0.7394	2.6180	0.5868
SAM&Lora Fine-Tuning	8	0.7598	2.1180	0.6127
SAM&Lora Fine-Tuning	16	0.7589	2.1180	0.6115
SAM&Lora Fine-Tuning	32	0.7558	2.2247	0.6076
SAM&Lora Fine-Tuning	64	0.7591	2.1180	0.6118
SAM&Lora Fine-Tuning	128	0.7624	2.1180	0.6160
SAM&Lora Fine-Tuning	256	0.7624	2.1180	0.6161

time-consuming to obtain. Furthermore, Low-Rank Adaptation (LoRA) played a crucial role in efficiently fine-tuning the SAM model for specific tasks. The choice of LoRA rank balanced model performance with computational efficiency, with higher ranks being beneficial for complex datasets, while lower ranks sufficed for simpler

tasks. This adaptability makes LoRA an attractive option for deploying medical AI systems in resource-constrained environments.

Synthetic data generation also proved beneficial, providing diverse pre-training data that closely resembled the original datasets. The use of

Table 16: Evaluation of generated transfer datasets using diffusion Models on multiple medical imaging tasks.

Dataset (Transfer)	PSNR (dB)	MSE
KidneyUS Transfer	27.7475	109.4084
Autooral Transfer	27.9109	105.2627
Chaos Transfer	27.6902	111.4721
PH2 Transfer	27.8803	105.9977
DRIVE Transfer	27.9510	104.4108

Swin-transformer-based diffusion models for generating synthetic images enabled robust augmentation across various medical imaging modalities. Increasing the size of the transfer dataset generally improved model performance, though diminishing returns were noted beyond a certain threshold, emphasizing the need for a balanced approach to data generation.

In comparison to self-supervised pretraining methods like MoCo v3 [29] and MAE [30], task-specific KD demonstrated superior performance, especially when labeled data was scarce. Self-supervised methods often fall short of capturing the detailed structural information required for medical segmentation, which limits their utility in tasks where domain-specific knowledge is crucial. In contrast, task-specific KD leverages pre-trained models to infuse rich semantic information tailored to the task, making it highly effective for medical applications.

Our approach, combining pretraining on synthetic data with task-specific KD, also demonstrated efficiency in training. Despite requiring more computational resources than some self-supervised methods, the performance gains justified the added complexity. The training pipeline allowed for pre-training on synthetic data, followed by efficient fine-tuning, providing a scalable solution for real-world medical segmentation tasks, where timely and accurate decision-making is paramount.

However, several limitations warrant further research. The reliance on synthetic data may introduce biases that affect generalization to real clinical settings. Future studies should aim to validate these findings across broader, real-world datasets and explore alternative augmentation techniques. Additionally, the trade-offs between model size and segmentation accuracy should

be further examined, potentially exploring other architectures or distillation methods that could offer similar or better performance without additional computational burden. Finally, applying our approach to more complex, multi-class segmentation tasks is an exciting direction for future work, as this could further showcase the benefits of transferring fine-grained anatomical knowledge.

In conclusion, our study underscores the potential of task-specific KD, combined with LoRA fine-tuning and synthetic data generation, to improve medical image segmentation, particularly in data-scarce environments significantly. This approach strikes an optimal balance between performance and computational efficiency, offering a viable pathway for scalable deployment in clinical practice, such as handling varying imaging modalities and adapting to new segmentation tasks. As the demand for efficient medical image analysis grows, the ability to adapt large models to specific tasks through distillation and fine-tuning will be increasingly crucial for advancing medical AI systems.

Data Availability

The datasets utilized in this study are all publicly accessible. The KidneyUS [45], Autooral [46], CHAOS [47], PH2 [48], and DRIVE [49] datasets can be obtained from their respective sources, each providing detailed annotations suited to their specific medical imaging tasks. These datasets support reproducibility and further exploration of segmentation techniques in diverse medical imaging modalities.

References

- [1] Liang, P., Chen, J., Yao, L., Yu, Y., Liang, K., Chang, Q.: Dawtran: dynamic adaptive windowing transformer network for pneumothorax segmentation with implicit feature alignment. *Physics in Medicine & Biology* **68**(17), 175020 (2023)
- [2] Abut, S., Okut, H., Kallail, K.J.: Paradigm shift from artificial neural networks (anns) to deep convolutional neural networks (dcnns)

- in the field of medical image processing. *Expert Systems with Applications*, 122983 (2023)
- [3] Munia, A.A., Abdar, M., Hasan, M., Jalali, M.S., Banerjee, B., Khosravi, A., Hossain, I., Fu, H., Frangi, A.F.: Attention-guided hierarchical fusion u-net for uncertainty-driven medical image segmentation. *Information Fusion*, 102719 (2024)
- [4] Li, L., Liu, J., Chen, S., Wang, J., Li, Y., Liao, Q., Zhang, L., Peng, X., Pu, X.: Segmentation of acute ischemic stroke lesions based on deep feature fusion. *Information Fusion*, 102724 (2024)
- [5] Pu, B., Li, K., Li, S., Zhu, N.: Automatic fetal ultrasound standard plane recognition based on deep learning and iiot. *IEEE Transactions on Industrial Informatics* **17**(11), 7771–7780 (2021)
- [6] Tajbakhsh, N., Jeyaseelan, L., Li, Y., Chiang, J.N., Wu, Z., Ding, X.: Embracing imperfect datasets: A review of deep learning solutions for medical image segmentation. *Medical Image Analysis* **63**, 101693 (2020)
- [7] Oquab, M., Darcet, T., Moutakanni, T., Vo, H., Szafraniec, M., Khalidov, V., Fernandez, P., Haziza, D., Massa, F., El-Nouby, A., et al.: Dinov2: Learning robust visual features without supervision. arXiv preprint arXiv:2304.07193 (2023)
- [8] Kirillov, A., Mintun, E., Ravi, N., Mao, H., Rolland, C., Gustafson, L., Xiao, T., Whitehead, S., Berg, A.C., Lo, W.-Y., et al.: Segment anything. In: Proceedings of the IEEE/CVF International Conference on Computer Vision, pp. 4015–4026 (2023)
- [9] Chen, C., Miao, J., Wu, D., Zhong, A., Yan, Z., Kim, S., Hu, J., Liu, Z., Sun, L., Li, X., et al.: Ma-sam: Modality-agnostic sam adaptation for 3d medical image segmentation. *Medical Image Analysis* **98**, 103310 (2024)
- [10] Zhang, Y., Zhou, T., Wang, S., Liang, P., Zhang, Y., Chen, D.Z.: Input augmentation with sam: Boosting medical image segmentation with segmentation foundation model. In: International Conference on Medical Image Computing and Computer-Assisted Intervention, pp. 129–139 (2023). Springer
- [11] Wang, C., Chen, H., Zhou, X., Wang, M., Zhang, Q.: Sam-ie: Sam-based image enhancement for facilitating medical image diagnosis with segmentation foundation model. *Expert Systems with Applications* **249**, 123795 (2024)
- [12] Leng, T., Zhang, Y., Han, K., Xie, X.: Self-sampling meta sam: enhancing few-shot medical image segmentation with meta-learning. In: Proceedings of the IEEE/CVF Winter Conference on Applications of Computer Vision, pp. 7925–7935 (2024)
- [13] Raghu, M., Zhang, C., Kleinberg, J., Bengio, S.: Transfusion: Understanding transfer learning for medical imaging. *Advances in Neural Information Processing Systems* **32** (2019)
- [14] Atasever, S., Azginoglu, N., Terzi, D.S., Terzi, R.: A comprehensive survey of deep learning research on medical image analysis with focus on transfer learning. *Clinical imaging* **94**, 18–41 (2023)
- [15] Messaoudi, H., Belaid, A., Salem, D.B., Conze, P.-H.: Cross-dimensional transfer learning in medical image segmentation with deep learning. *Medical image analysis* **88**, 102868 (2023)
- [16] Hinton, G., Vinyals, O., Dean, J.: Distilling the knowledge in a neural network. arXiv preprint arXiv:1503.02531 (2015)
- [17] Gou, J., Yu, B., Maybank, S.J., Tao, D.: Knowledge distillation: A survey. *International Journal of Computer Vision* **129**(6), 1789–1819 (2021)
- [18] Li, H., Zhou, Y., Zhao, Z., Du, S., Yao, J., Xie, W., Zhang, Y., Wang, Y.: Lorkd: Low-rank knowledge decomposition for medical foundation models. arXiv preprint arXiv:2409.19540 (2024)

- [19] Liang, P., Chen, J., Chang, Q., Yao, L.: Rskd: Enhanced medical image segmentation via multi-layer, rank-sensitive knowledge distillation in vision transformer models. *Knowledge-Based Systems* **293**, 111664 (2024)
- [20] Zhao, L., Qian, X., Guo, Y., Song, J., Hou, J., Gong, J.: Mskd: Structured knowledge distillation for efficient medical image segmentation. *Computers in Biology and Medicine* **164**, 107284 (2023)
- [21] Xiong, Y., Varadarajan, B., Wu, L., Xiang, X., Xiao, F., Zhu, C., Dai, X., Wang, D., Sun, F., Iandola, F., *et al.*: Efficientsam: Leveraged masked image pretraining for efficient segment anything. In: *Proceedings of the IEEE/CVF Conference on Computer Vision and Pattern Recognition*, pp. 16111–16121 (2024)
- [22] Hu, E.J., Shen, Y., Wallis, P., Allen-Zhu, Z., Li, Y., Wang, S., Wang, L., Chen, W.: Lora: Low-rank adaptation of large language models. *arXiv preprint arXiv:2106.09685* (2021)
- [23] Yan, X., Sun, S., Han, K., Le, T.-T., Ma, H., You, C., Xie, X.: After-sam: Adapting sam with axial fusion transformer for medical imaging segmentation. In: *Proceedings of the IEEE/CVF Winter Conference on Applications of Computer Vision*, pp. 7975–7984 (2024)
- [24] Cheng, Z., Wei, Q., Zhu, H., Wang, Y., Qu, L., Shao, W., Zhou, Y.: Unleashing the potential of sam for medical adaptation via hierarchical decoding. In: *Proceedings of the IEEE/CVF Conference on Computer Vision and Pattern Recognition*, pp. 3511–3522 (2024)
- [25] Wang, X., Ye, F., Zhang, Y.: Task-aware low-rank adaptation of segment anything model. *arXiv preprint arXiv:2403.10971* (2024)
- [26] Ho, J., Jain, A., Abbeel, P.: Denoising diffusion probabilistic models. *Advances in Neural Information Processing Systems* **33**, 6840–6851 (2020)
- [27] Kawar, B., Elad, M., Ermon, S., Song, J.: Denoising diffusion restoration models. *Advances in Neural Information Processing Systems* **35**, 23593–23606 (2022)
- [28] Garcea, F., Serra, A., Lamberti, F., Morra, L.: Data augmentation for medical imaging: A systematic literature review. *Computers in Biology and Medicine* **152**, 106391 (2023)
- [29] Chen, X., Xie, S., He, K.: An empirical study of training self-supervised vision transformers. In: *Proceedings of the IEEE/CVF International Conference on Computer Vision*, pp. 9640–9649 (2021)
- [30] He, K., Chen, X., Xie, S., Li, Y., Dollár, P., Girshick, R.: Masked autoencoders are scalable vision learners. In: *Proceedings of the IEEE/CVF Conference on Computer Vision and Pattern Recognition*, pp. 16000–16009 (2022)
- [31] Zheng, H., Han, J., Wang, H., Yang, L., Zhao, Z., Wang, C., Chen, D.Z.: Hierarchical self-supervised learning for medical image segmentation based on multi-domain data aggregation. In: *Medical Image Computing and Computer Assisted Intervention—MICCAI 2021*, pp. 622–632 (2021). Springer
- [32] Miao, J., Zhou, S.-P., Zhou, G.-Q., Wang, K.-N., Yang, M., Zhou, S., Chen, Y.: Sc-ssl: Self-correcting collaborative and contrastive co-training model for semi-supervised medical image segmentation. *IEEE Transactions on Medical Imaging* (2023)
- [33] Pani, K., Chawla, I.: A hybrid approach for multi modal brain tumor segmentation using two phase transfer learning, ssl and a hybrid 3dunet. *Computers and Electrical Engineering* **118**, 109418 (2024)
- [34] Yan, R., Qu, L., Wei, Q., Huang, S.-C., Shen, L., Rubin, D.L., Xing, L., Zhou, Y.: Label-efficient self-supervised federated learning for tackling data heterogeneity in medical imaging. *IEEE Transactions on Medical Imaging* **42**(7), 1932–1943 (2023)
- [35] Zhang, L., Shi, Y., Shi, Z., Ma, K., Bao, C.:

- Task-oriented feature distillation. *Advances in Neural Information Processing Systems* **33**, 14759–14771 (2020)
- [36] Heo, B., Kim, J., Yun, S., Park, H., Kwak, N., Choi, J.Y.: A comprehensive overhaul of feature distillation. In: *Proceedings of the IEEE/CVF International Conference on Computer Vision*, pp. 1921–1930 (2019)
- [37] Liu, M., Chen, X., Zhang, Y., Li, Y., Rehg, J.M.: Attention distillation for learning video representations. *arXiv preprint arXiv:1904.03249* (2019)
- [38] Guo, Z., Yan, H., Li, H., Lin, X.: Class attention transfer based knowledge distillation. In: *Proceedings of the IEEE/CVF Conference on Computer Vision and Pattern Recognition*, pp. 11868–11877 (2023)
- [39] Zhang, J., Huang, J., Jin, S., Lu, S.: Vision-language models for vision tasks: A survey. *IEEE Transactions on Pattern Analysis and Machine Intelligence* (2024)
- [40] Sameni, S., Kafle, K., Tan, H., Jenni, S.: Building vision-language models on solid foundations with masked distillation. In: *Proceedings of the IEEE/CVF Conference on Computer Vision and Pattern Recognition*, pp. 14216–14226 (2024)
- [41] Kornblith, S., Shlens, J., Le, Q.V.: Do better imagenet models transfer better? In: *Proceedings of the IEEE/CVF Conference on Computer Vision and Pattern Recognition*, pp. 2661–2671 (2019)
- [42] Su, Z., Yao, K., Yang, X., Huang, K., Wang, Q., Sun, J.: Rethinking data augmentation for single-source domain generalization in medical image segmentation. In: *Proceedings of the AAAI Conference on Artificial Intelligence*, vol. 37, pp. 2366–2374 (2023)
- [43] Zhang, K., Liu, D.: Customized segment anything model for medical image segmentation. *arXiv preprint arXiv:2304.13785* (2023)
- [44] Pan, S., Wang, T., Qiu, R.L., Axente, M., Chang, C.-W., Peng, J., Patel, A.B., Shelton, J., Patel, S.A., Roper, J., *et al.*: 2d medical image synthesis using transformer-based denoising diffusion probabilistic model. *Physics in Medicine & Biology* **68**(10), 105004 (2023)
- [45] Singla, R., Ringstrom, C., Hu, G., Lessoway, V., Reid, J., Nguan, C., Rohling, R.: The open kidney ultrasound data set. In: *International Workshop on Advances in Simplifying Medical Ultrasound*, pp. 155–164 (2023). Springer
- [46] Jiang, C., Wu, R., Liu, Y., Wang, Y., Chang, Q., Liang, P., Fan, Y.: A high-order focus interaction model and oral ulcer dataset for oral ulcer segmentation. *Scientific Reports* **14**(1), 20085 (2024)
- [47] Kavur, A.E., Gezer, N.S., Barış, M., Aslan, S., Conze, P.-H., Groza, V., Pham, D.D., Chatterjee, S., Ernst, P., Özkan, S., *et al.*: Chaos challenge-combined (ct-mr) healthy abdominal organ segmentation. *Medical Image Analysis* **69**, 101950 (2021)
- [48] Mendonça, T., Celebi, M., Mendonca, T., Marques, J.: Ph2: A public database for the analysis of dermoscopic images. *Dermoscopy image analysis* **2** (2015)
- [49] Staal, J., Abràmoff, M.D., Niemeijer, M., Viergever, M.A., Van Ginneken, B.: Ridge-based vessel segmentation in color images of the retina. *IEEE transactions on medical imaging* **23**(4), 501–509 (2004)
- [50] Dosovitskiy, A., Beyer, L., Kolesnikov, A., Weissenborn, D., Zhai, X., Unterthiner, T., Dehghani, M., Minderer, M., Heigold, G., Gelly, S., Uszkoreit, J., Houslyby, N.: An image is worth 16x16 words: Transformers for image recognition at scale. *ICLR* (2021)
- [51] Wang, S., Gao, J., Li, Z., Zhang, X., Hu, W.: A closer look at self-supervised lightweight vision transformers. In: *International Conference on Machine Learning*, pp. 35624–35641 (2023). PMLR